CHALMERS
UNIVERSITY OF TECHNOLOGY

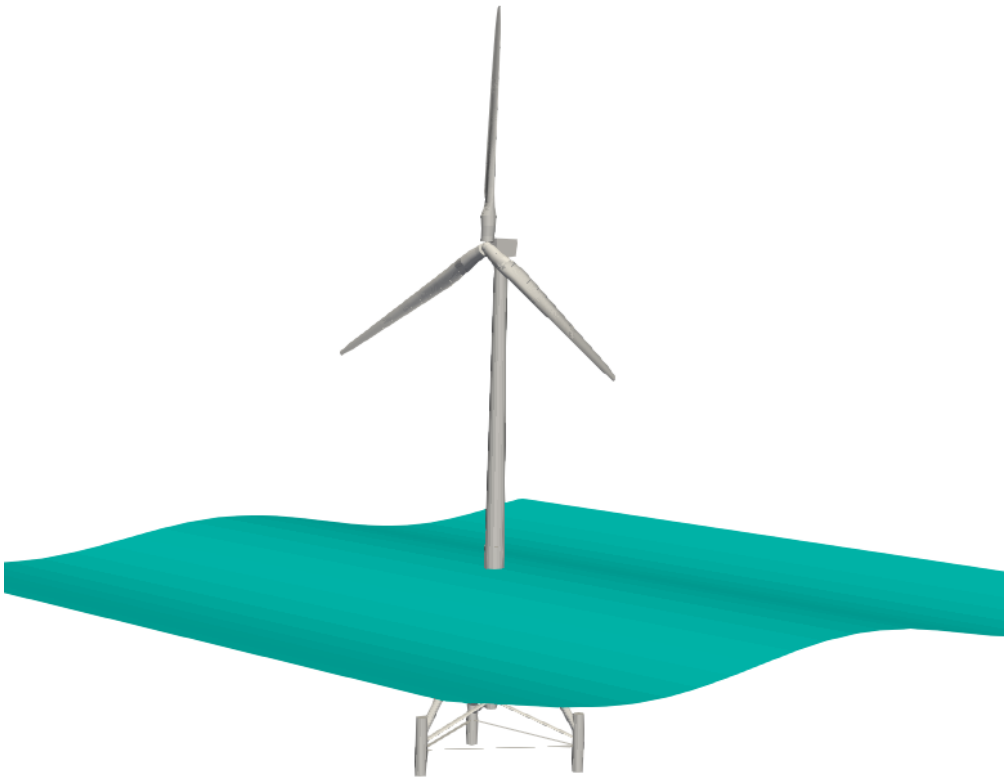

Assessment of the Potential and Current Limitations of Integrating CFD and Structural Analyses for the Design of Offshore Wind Turbines

Master's thesis in Applied Mechanics

Julius Kandt

Department of Mechanics and Maritime Sciences
CHALMERS UNIVERSITY OF TECHNOLOGY
Gothenburg, Sweden 2019

Master's thesis 2019:25

Assessment of the Potential and Current Limitations of Integrating CFD and Structural Analyses for the Design of Offshore Wind Turbines

Julius Kandt

CHALMERS
UNIVERSITY OF TECHNOLOGY

Department of Mechanics and Maritime Sciences
Division of Fluid Dynamics
Chalmers University of Technology
Gothenburg, Sweden

Assessment of the Potential and Current Limitations of Integrating CFD and Structural Analyses for the Design of Offshore Wind Turbines

Supervisor: Hamidreza Abedi, Division of Fluid Dynamics
Examiner: Lars Davidson, Division of Fluid Dynamics

Master's Thesis 2019:25
Department of Mechanics and Maritime Sciences
Division of Fluid Dynamics
Chalmers University of Technology
SE-412 96 Gothenburg
Telephone +46 31 772 1000

Cover: Visualization of a *FAST* simulation of an offshore wind turbine with OC3 Tripod configuration.

Typeset in LaTeX
Gothenburg, Sweden 2019

Assessment of the Potential and Current Limitations of Integrating CFD and Structural Analyses for the Design of Offshore Wind Turbines
Julius Kandt
Department of Mechanics and Maritime Sciences
Chalmers University of Technology

Abstract

While the need for electric energy grows over the years, the environmental impact is an important factor for the energy generation as well. Wind power plays a major role among the renewable energies nowadays. However, the available space onshore is restricted and complex terrain complicates the use of various areas even more. Among others this is one of the reasons why the use of offshore wind power stations becomes more attractive.
Therefore, the assessment of offshore sites is an important aspect that may decide whether to place a wind plant or not. For this Computational Fluid Dynamics have become a popular approach over the past years replacing simpler spectral methods. In this study the modeling of the Atmospheric Boundary Layer for the generation of an offshore environment using a Large Eddy Simulation was investigated. Overall it was found, that this method is able to reproduce the Atmospheric Boundary Layer well, especially when it comes to the mean velocity field. Nevertheless, inaccuracies were found considering the Reynolds stresses, especially the shear components.
Moreover, the flow field obtained with the Large Eddy Simulation was compared to a spectral flow field and the dynamic response of two wind turbines was assessed using the aero-elastic solver *FAST*. The results of both methods are in close agreement to each other. Therefore, the integration of the aero-elastic solver *FAST* into the process of an analysis using Computational Fluid Dynamics works well.
Finally, the performance of the Actuator Disk and Actuator Line model was tested in *Star-CCM+*. The effect of these models on the flow field was investigated as well as the thrust and torque calculation. It was found that both models do not match the *FAST* results very well in terms of the torque prediction. However, the thrust calculation of the Actuator Line Model comes close to the results from *FAST*. Several aspects were outlined for further investigation.

Keywords: Wind turbine, Offshore, Atmospheric Boundary Layer, Large Eddy Simulation, Actuator Disk Model, Actuator Line Model, *FAST*

Acknowledgements

I would like to thank all the people that made this thesis possible for all their input and suggestions for improvements. Most of all I want to thank my supervisor Hamidreza Abedi. He has been very supportive throughout the entire project, providing valuable input and inspiring with his ideas. Furthermore, I would like to thank Lars Davidson and the Division of Fluid Dynamics, who made this project possible in the first place. Finally, I would like to thank my family and friends, who supported and encouraged me the entire time.

Julius Kandt, Gothenburg, June 2019

Contents

List of Figures

List of Tables

Nomenclature

Abbreviations

ABL	Atmospheric boundary layer.	LES	Large Eddy Simulation.
ADM	Actuator Disk Model.	MABL	Marine Atmospheric Boundary Layer.
ALM	Actuator Line Model.	NREL	National Renewable Energy Laboratory.
AOA	Angle Of Attack.	NS	Navier-Stokes.
BEM	Blade-Element-Momentum.	RANS	Reynolds-Averaged Navier-Stokes.
CFD	Computational Fluid Dynamics.	SGS	Subgrid-Scales.
DES	Detached Eddy Simulation.	SST	Shear Stress Transport.
DNS	Direct Numerical Simulation.	TSR	Tip-Speed Ratio.
DSM	Dynamic Smagorinsky Model.	URANS	Unsteady Reynolds-Averaged Navier-Stokes.
FAST	Fatigue, Aerodynamics, Structures and Turbulence.	WAsP	Wind Atlas Analysis and Application Program.

Subscripts

$_0$	Free stream.	$_{norm}$	Normal component.
$_1$	Far wake.	$_{out}$	Outer disk.
$_{i,\ ij}$	Einstein summation notation.	$_{ref}$	Reference value.
$_k$	Turbulent kinetic energy.	$_{rel}$	Relative with respect to a blade.
$_t$	Turbulent quantity.	$_{tang}$	Tangential component.
$_{in}$	Inner disk.		

Greek Letters

α_t	Thermal diffusion	$[\frac{m^2}{s}]$	δ_{ij}	Kroenecker's δ	$[-]$
β	Inflow angle	$[^\circ]$	ϵ	Turbulent dissipation	$[\frac{m^2}{s^3}]$
Δ	Filter width	$[m]$	η	Kolmogorov microscale	$[m]$
δ	Actuator disk thickness	$[m]$	κ	Wavenumber	$[m^{-1}]$

κ_w	von Kármán constant	$[-]$	Ω	Rotational rotor speed	$[\frac{rad}{s}]$
Λ	Turbulent length scale	$[m]$	ω	Induction angular velocity	$[\frac{rad}{s}]$
λ	Tip-speed ratio	$[-]$	ρ	Density	$[\frac{kg}{m^3}]$
μ	Dynamic viscosity	$[\frac{kg}{ms}]$	σ	Solidity	$[-]$
ν	Kinematic viscosity	$[\frac{m^2}{s}]$	σ_k	Turbulent Prandtl number	$[-]$
ν_e	Subgrid-scale eddy viscosity coefficient	$[\frac{m^2}{s}]$	σ_ϵ	Model constant for the k-ϵ model	$[-]$
ν_t	Turbulent viscosity	$[\frac{m^2}{s}]$	τ_{ij}	Reynolds stress tensor	$[\frac{kg}{ms^2}]$
			$\widetilde{\tau_{ij}}$	Subgrid-scale stress tensor	$[\frac{m^2}{s^2}]$

Roman Letters

a	Axial induction factor	$[-]$	l_m	Mixing length	$[m]$
A	Section area	$[m^2]$	L	Lift force	$[\frac{kgm}{s^2}]$
b	Tangential induction factor	$[-]$	m	Mass element	$[kg]$
c	Chord length	$[m]$	p	Hydrodynamic pressure	$[\frac{kg}{ms^2}]$
$c_{\epsilon 1}$, $c_{\epsilon 2}$, c_μ	Model constants for the k-ϵ model	$[-]$	Q	Torque	$[\frac{kgm^2}{s^2}]$
C	Wall function constant	$[-]$	r	Radius	$[m]$
C_d	Drag coefficient	$[-]$	r_h	Roughness height	$[m]$
C_l	Lift coefficient	$[-]$	R	Correlation coefficient	$[-]$
C_s	Smagorinsky constant	$[-]$	Re	Reynolds number	$[-]$
C_t	Thrust coefficient	$[-]$	Re_{ii}	Normal components of the Reynolds stresses	$[\frac{m^2}{s^2}]$
C_K	Kolmogorov constant	$[-]$	Re_{ij}	Shear components of the Reynolds stresses	$[\frac{m^2}{s^2}]$
D	Drag force	$[\frac{kgm}{s^2}]$	t	Time	$[s]$
$\tilde{D}_{ij}$	grid-scale rate-of-strain tensor	$[-]$	T	Thrust force	$[\frac{kgm}{s^2}]$
E	Energy density spectrum	$[\frac{m^2}{s^2}/Hz]$	u	Characteristic velocity in a steady state	$[\frac{m}{s}]$
E_C	Wall function constant	$[-]$	u'	Fluctuation velocity	$[\frac{m}{s}]$
F	Force	$[\frac{kgm}{s^2}]$	u_*	Friction velocity	$[\frac{m}{s}]$
I	Turbulence intensity	$[-]$	v_i	Velocity component	$[\frac{m}{s}]$
k	Turbulent kinetic Energy	$[\frac{m^2}{s^2}]$	V	Axial velocity	$[\frac{m}{s}]$
l	Characteristic length	$[m]$	x_i	Cartesian coordinate	$[-]$
			y_0	Roughness length	$[m]$

1
Introduction

Due to a significant growth in the worlds population the need for electric energy increased rapidly over the last decades. While fossil fuels such as coal, oil and natural gas built the foundation of the energy supply since the beginning of the industrial evolution, there have been various concerns about the impact of these resources on the environment in recent years [18]. Global challenges like the climate change, the emission of greenhouse gases and air pollution require a change in the worldwide energy production [35]. Although nuclear power does produce only low carbon dioxide emissions, the question of what to do with radioactive waste is still not solved and a topic of huge controversies [12].
Hence, the development of sustainable and clean energies is a matter of interest in many regions all over the world. Among multiple forms of renewable energies, wind power plays an important role and is considered the most sustainable renewable energy technique [16]. Furthermore humans have used wind power for a long period of time and therefore a lot of expertise has been gathered.

1.1 Historical Background

While the use of wind power is almost 3000 years old, its purpose as generation of electric energy started about 120 years ago. Since then wind power had a continuous development in terms of its technology.
Although there always has been a dependency on oil prices, the electric capacity of wind power has been growing about 30 % per year over the last decade [2]. In fact there are predictions, that wind energy will generate about 5 % of the worlds energy demand in 2020 [19]. As one of its inventors Germany is one of the leading countries in terms electric energy production using wind power. The fraction of renewable energies was about 38.2 % net in 2017 and wind power provided about 18.8 % of the total net electric energy production [6][15].
In terms of the use of renewable energies Sweden is even more advanced. In this matter it leads the European Union and reached its target of producing half of its energy from renewable sources in 2012. In 2018 about 54 % came from renewable energy sources and about 11 % from wind power [46].

In order to generate more electricity, wind power stations are growing to larger scales. In the period from 2010 to 2017 the average power produced by a wind turbine increased from 1.77 MW to 2.7 MW [14]. However the space available onshore is limited or may have a difficult topography.

This is one of the reasons offshore wind is an attractive alternative. Moreover there are several other advantages. The sites available offshore may not only be used to increase the number of wind turbines but also to enhance their size. Furthermore the impact on human life is much less. Hence the focus on development may be more efficiency orientated without the concern of noise emission or visual disturbances [5]. Another key fact is that offshore winds often blow stronger and more uniform than onshore. This may reduce the stresses on the turbine induced by the wind. Additionally the energy production indicator for offshore wind power stations is around 4000 full load hours per year, while it is around 2000-2500 for onshore sites [30]. Nevertheless there is still development necessary in order to reduce the high costs for offshore wind power stations, which are around 50 % higher than onshore [30].

To improve the performance and expand the lifetime of wind power stations numerous experiments have been conducted over the last decades. In addition computational calculation and prediction methods have also improved among others due to increasing computing power. Multiple programs were invented, one of the most commonly used is *Wind Atlas Analysis and Application Program (WAsP)* [34], which is based on the wind-atlas model [47]. This model solves linearised fluid equations, which cannot resolve detached flow or recirculation. While it performs well on flat terrain, it tend to have problems with complex terrain or when analyzing bigger wind farms [7] which is one of the main interest in today's research.

However, since computational power became more affordable Computational Fluid Dynamics (CFD) has been applied to wind energy research to refine the results and increase accuracy. Since CFD is a non-linear method it makes it possible to capture wake effects. This is especially important for the efficiency of large-scale wind farms, as one can assess the interactions between the turbines with each other. Furthermore, it is important for the structural aspects as well. Therefore, it can affect the lifetime as well, which is a crucial point in terms of the costs.

1.2 Simulation Methods

Overall, there are various types of simulations available today for assessing wind fields, the response of wind turbines as well as predicting the power outcome. Besides linear applications like *WAsP* nonlinear CFD methods are becoming more common, especially for evaluating the effect of complex terrain and wake assessment on single turbines and wind parks.

Currently two different CFD methods are in use. On the one hand, there are the time averaged models, e.g. Reynolds-Averaged Navier-Stokes (RANS) models and on the other the time resolved approaches, e.g. Large Eddy Simulation (LES). Furthermore, so-called Hybrid methods are becoming more popular. They combine different methods, e.g. RANS and LES. The full resolving Direct Numerical Simulation (DNS) is still too power demanding to have actual use in wind engineering. This is mainly caused by the large variety of scales in the Atmospheric Boundary

Layer (ABL) and will be discussed later on. However, since atmospheric flow is a turbulent and therefore time depending phenomenon, LES is a promising approach, especially with regard to the development of the computer power.

Furthermore, CFD methods have been developed to assess the influence of one or more wind turbines on the flow field without actually resolving the turbine geometry. Two of these methods used in the present study are the so-called Actuator Disk Model (ADM) and Actuator Line Model (ALM). It is possible to study the flow field of single turbines or multiple turbine up to whole wind parks.

Besides the flow assessment another important aspect is the impact of the flow on the wind turbine. Determining the response of the wind turbine to the loads and stresses induced by the wind is a crucial aspect for the design of the structure and lifetime. A popular approach for the combined use with CFD software is Blade-Element-Momentum (BEM) theory, which is a combination of two different methods itself (blade element and momentum theory).

1.3 Literature Review

The modeling of the ABL has been the objective of various studies. One of the most popular approaches for modeling the mean flow with the k-ϵ model was proposed by Richards and Hoxey [38]. They derived the inlet conditions analytically so that they fulfill the governing equations of the k-ϵ model. This produces a homogeneous flow field throughout the domain. Hargreaves and Wright [17] improved this model by applying shear stresses at the top of the domain. This leads to better results, especially for the turbulent kinetic energy. Other modifications were made by Parente and Benocci [36], who introduced additional source terms to the transport equations of the turbulent kinetic energy and the turbulent dissipation.

For transient modeling of the ABL Porté-Agel et. al. [37] published a well-known article assessing different subgrid-scale models for LES. Comparing the introduced scale-dependent dynamic model with the standard Smagorinsky model and the original dynamic model he found improvements in terms of dissipative properties, especially in near wall regions. Furthermore, Vasaturo et. al. [48] investigated different inflow methods for LES. They conclude, that the most accurate method is the precursor method, which means running a precursor simulation to obtain the inflow quantities.

To model especially the wake behind turbines and wind farms Stevens et. al. [44] studied the performance of the ADM and ALM and compared the results with wind tunnels experiments. In contrast to earlier results they concluded that both the ADM and ALM are capable of reproducing accurate results, especially if the nacelle and tower effects are included. Furthermore, the ALM is assumed to have its advantages over the ADM, that is the resolution of tip vortices and radial distribution alongside the blades, only in high resolution grids. This is also validated by Churchfield et. al. [9] and other researchers [40][53]. Moreover, Martínez et. al.

investigated the influence of the mesh resolution on the predicted power output of both models and conclude that the power decreases with the number of cells [31].

1.4 Objectives and limitations

The main objective of this thesis is to study the potential and current limitations of integrating CFD methods and structural analysis for the design of offshore wind turbines. This main objective can be structured in three different aims. The first one is the generation of a transient flow field through LES for further investigations. To obtain a transient flow field with good quality, one needs to create a mean velocity field and describe the turbulence characteristics as input parameters for the LES. In the present study this is done with a RANS simulation. Once the transient flow field is obtained it can be transmitted to *FAST* for aero-elastic assessment. Then it will be compared to the original spectral input. Finally, integrated CFD methods like the ADM and ALM will be investigated and compared to the *FAST* simulation.

The following list gives an overview over the detailed objectives of this thesis.

- Set up of a RANS simulation to simulate the ABL with good accuracy and agreement with the current theoretical models and literature.
- Perform a LES to produce a transient flow field. Compare this flow field to previous RANS simulation and literature.
- Transmit the flow field for two different turbine locations to *FAST* and perform aero-elastic simulations for each turbine. Compare the turbines to each other and the original spectral flow field as input.
- Perform a LES with the ADM and ALM applied to it, respectively. Assess the influence of the respective models on the flow field. Compare the turbines and investigate the influence of the first turbine on the second. Calculate force and momentum outputs and compare them with the *FAST* simulation.

Nevertheless, there are some limitations to the present study. The limitations for the CFD calculations are mainly the computational resources as well as the models and possibilities available in the CFD software *Star-CCM+* and the aero-elastic solver *FAST*. Further on the project is limited by the time available to prepare and assess the simulations.

2

Theory

In this chapter the theoretical foundation of the thesis is discussed. Therefore, the Atmospheric Boundary Layer (ABL) and its different conditions are described, as it is one of the main parts of this investigation. Fundamental basics like structure and fluid motions within the ABL as well as differences between on- and offshore wind plants are outlined. Moreover, the concept of Computational Fluid Dynamics (CFD) is presented including different models used in this thesis. The governing equations are derived and the mathematical description of turbulence and how to deal with it is shown. Furthermore the basic aerodynamics of wind turbine rotors are presented as well as the fundamental theory for aerodynamic analysis methods with the BEM approach are outlined. Finally the reference turbine used in this thesis is described.

2.1 Atmospheric Boundary Layer

The ABL surrounds the earth's surface and extends to 10-20 % of the troposphere. It is defined as the part of the troposphere that is influenced by the earth's surface [27][50]. Its height differs dramatically from tens of meters up to 4 km [50], depending on various boundary conditions, see e.g. sub-section 2.1.1. Furthermore, the thickness of the ABL varies with time and space, as shown in figure 2.1.

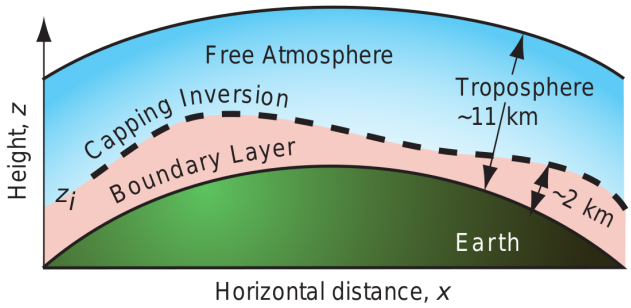

Figure 2.1: Thickness of the Atmospheric Boundary Layer. Figure taken from [50]

The ABL can be divided into three different regions, as figure 2.2 shows. One can see the roughness sublayer next to the ground, followed by the constant-flux or Prandtl sublayer and finally the Ekman sublayer. Within the roughness sublayer one can also find the laminar or viscous sublayer adjacent to the surface. It measures only a few millimeters and is therefore too thin to be shown in figure 2.2. The Prandtl sublayer is meteorologically defined as the layer, where the turbulent vertical momentum

flux, heat and moisture deviate less than 10 % from their surface values and the influence of the Coriolis force is negligible. Usually it covers about 10 % of the total ABL thickness. However, modern wind turbines tend to exceed the Prandtl layer and reach into the Ekman layer. One of the main differences between these two sublayers is that the Coriolis force can not be neglected [13]. How to mathematically describe the velocities in the ABL and within the different layers is discussed in sub-section 2.2.6.

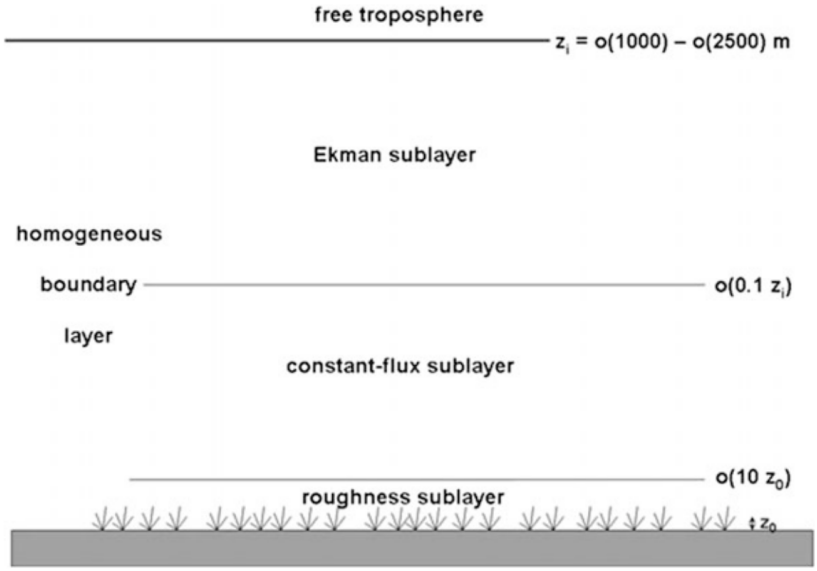

Figure 2.2: Vertical structure of the Atmospheric Boundary Layer. Figure taken from [13]

2.1.1 Onshore Atmospheric Stability

The atmospheric stability status has great influence on the extend of the ABL. Usually the stability changes depending on the temperature difference between the earth's surface and the surrounding fluid [50]. A typical cycle during fair weather (which means no precipitation or clouds and moderate wind speeds) conditions over land can be seen in figure 2.3.

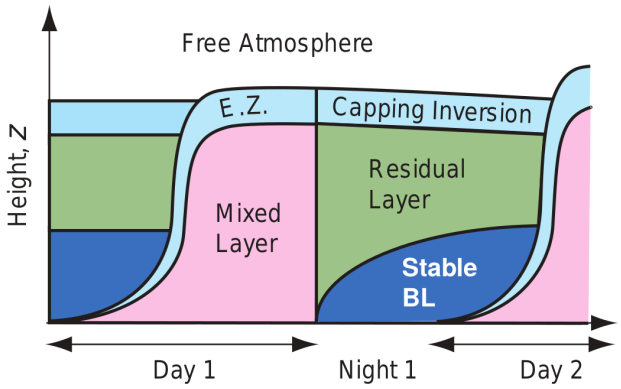

Figure 2.3: Typical diurnal cycle of the Atmospheric Boundary Layer during fair weather. Figure taken from [50]

After the sun rises, the surface heats up and the mixed layer grows due to heat convection. Therefore, it is also called the convective boundary layer. Strong vertical mixing takes place in this layer, thus the vertical gradients are small. Moreover, entrainment occurs, because the mixed layer is expanding, hence inducing fluid motion in the surrounding air. This entrainment region also builds the capping inversion, which is the top end of the ABL. When the sun sets and the ground cools down and the stable boundary layer develops. Here the vertical mixing is not very distinct and therefore vertical gradients are higher than in the mixed layer. Above the stable boundary layer the residual layer occurs, as it is a remnant from the mixed layer during the daytime [50].
In total there are three different stability states for the ABL. The state is categorized as unstable if the surface is warmer than its surroundings and therefore heating up the air. This is because of the corresponding change in the air's density and resulting fluid motions. The air closer to the ground heats up, the density sinks and as a consequence the warmer air ascents to greater heights. During its way up the air cools down and sinks to the ground again. As a result the vertical convection in the ABL is very high, turbulence is produced and the boundary layer is well mixed. Also the ABL total thickness increases. This is typically the case during daytime. On the contrary the ground is often colder than the air during nighttime and this state is defined as a stable boundary layer, because no fluid motion is induced by cooling the air adjacent to the ground. Finally the ABL is called neutral, if the potential temperature is constant with height. Typically this is only a short period of time at late afternoon [27].

The stability has great influence on the velocity profile of the wind, as it can be seen in figure 2.4. Because of the highest vertical convection the unstable ABL has also the highest velocity gradient near the ground. After only a short vertical distance the velocity profile is fairly uniform. On the opposite side the stable ABL has the lowest velocity gradient and the neutral ABL lies somewhere in between [50].

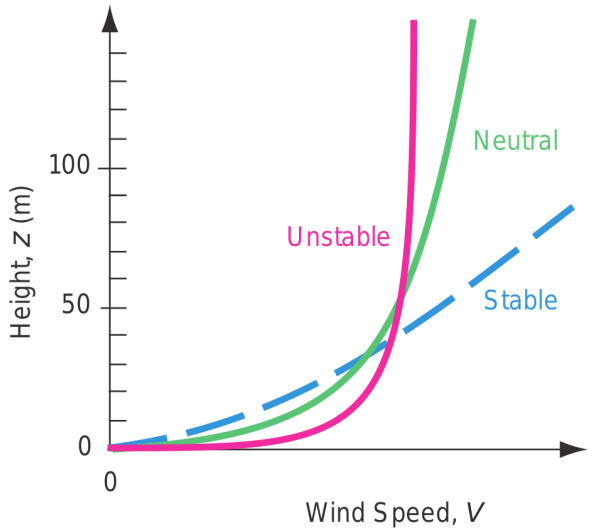

Figure 2.4: Variation of wind speed due to atmospheric stability. Figure adapted from [50]

2.1.2 Marine Atmospheric Boundary Layer

The Marine Atmospheric Boundary Layer (MABL) is somewhat different from the onshore ABL. One of the main differences is the roughness length, which is much less for the offshore, since the surface is much smoother than onshore flat terrain. As a consequence offshore wind speeds at a given height are much higher, the turbulence intensity is less and the thickness of the surface layer is smaller as well. Less turbulence often leads to less shear over the wind turbine. In contrast to the onshore characteristics, the offshore roughness length is dependent on the wind speed because of the wave influence (it increases with the wind speed). Also the diurnal cycle is nearly absent due to large thermal storage capacities of the sea [13].

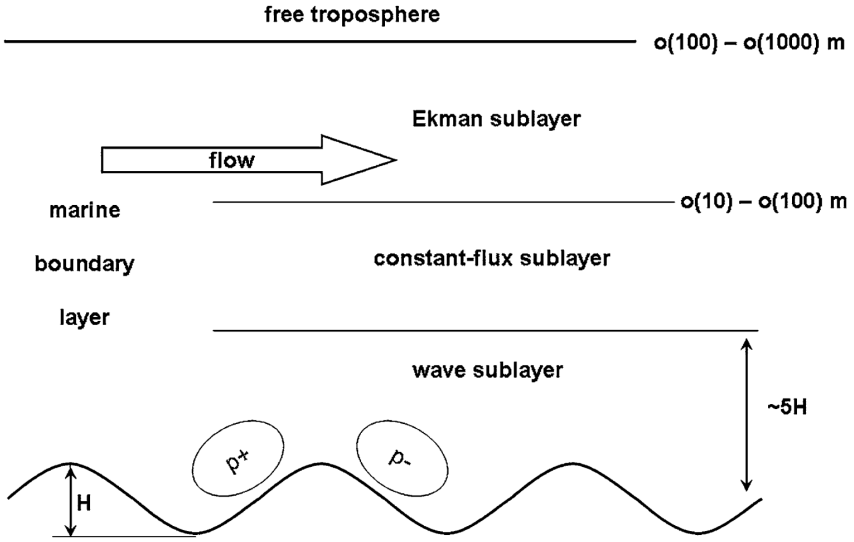

Figure 2.5: Structure of the Marine Atmospheric Boundary Layer. Figure taken from [13]

The vertical structure of the MABL is shown in figure 2.5. Adjacent to the surface there is the wave sublayer, which is directly influenced by single waves due to the dominant pressure forces. The wave sublayer is usually about five wave amplitudes deep. Above that one can find the constant-flux sublayer or Prandtl layer. This layer is, as the entire MABL, much shallower than the ABL over land. The Ekman sublayer represents the upper 90 % of the MABL and then turns into geostrophic wind. Note, that the change in wind speed at hub height in the present study occurs within the Ekman layer and therefore the same law for the mean wind speed as for onshore wind turbines can be used [13]. This is discussed later on in section 2.2.6.

2.2 Computational Fluid Dynamics (CFD)

CFD is the computer-based simulation and assessment of systems with fluid flow, heat transfer and other associated phenomena e.g. chemical reactions [49]. It is a powerful technique that can be used in a large variety of applications and industries.

2.2.1 Historical Background

The industrial beginnings of CFD reach back into the 1960s, where the aerospace industry first integrated CFD into the design of aircraft and jet engines. With the further development of CFD and more computer power available over the years, it was also used to design internal combustion engines, combustion chambers for gas turbines and furnaces. Nowadays even car manufacturers use CFD on a daily basis to predict essential physical characteristics, e.g. drag forces and even the interior car environment [49]. However, due to its complex problems and relations the capability of CFD is still a bit behind other computer aided engineering tools, e.g. stress analysis tools.

Despite the development, that still has to be made, there are various arguments in favor of using CFD summarized in the following list [42]:

- When trying to find an analytical solution for fluid mechanical problems, only highly simplified situations can be resolved. In some cases these simplifications do not represent the physical situation, leaving the initial problem unsolved.
- Although empirical relations might exist and be documented for some problems one can only adapt these relations for very similar situations.
- An experimental assessment is not possible in many flows due to different circumstances. The assessed fluid might be very hot or chemically aggressive and therefore the measurements devices might get destroyed while in contact with the fluid. When using invasive methods, the sensors might distort the results. On the opposite site non-contact method might not be applicable for the assessed flow, e.g. due to missing visibility and other reasons.
- In terms of costs CFD is getting more and more affordable due to the lowering cost for computer power, but the costs for experimental devices do not profit from such a phenomenon.
- It is often easier to conduct parameter studies in CFD than in experimental methods.

However, often both CFD and experimental analysis is used for obtaining best possible knowledge about a flow field. On the one hand experiments validate CFD analysis in certain situations, on the other hand, CFD can help to understand the flow field.

2.2.2 Navier-Stokes (NS) Equations

In the following sections the governing equations for the present study is introduced. For this, one presents the Navier-Stokes (NS) equations and then derive the Reynolds-Averaged Navier-Stokes (RANS) equations as well as the spatial filtered NS equations, the so-called Large Eddy Simulation (LES).
The NS equations describe four equations in total. One equation represents the conservation of mass, also known as the continuity equation. The three other equations describe the conservation of momentum in each direction. They are derived from Newton's second law applied to an element of fluid and a given mass.

The continuity equation for an incompressible fluid in Cartesian coordinates can be written as

$$\rho \frac{\partial v_i}{\partial x_i} = 0, \tag{2.1}$$

where ρ denotes the density, which is constant is this case [11].
The momentum equations with the Einstein summation notation[1] can be formulated as

$$\rho \frac{\partial v_i}{\partial t} + \rho \frac{\partial v_i v_j}{\partial x_j} = -\frac{\partial p}{\partial x_i} + \mu \frac{\partial^2 v_i}{\partial x_j \partial x_j}. \tag{2.2}$$

x_i is used for the Cartesian coordinate system as well, where $i = 1, 2$ or 3 for x, y or z, while v_i denotes the velocity field with $i = 1, 2$ or 3 for u, v or w. The hydrodynamic pressure is represented by p, the dynamic viscosity by μ [11]. Note that μ is constant in the present case and the external forces acting on the fluid element have been neglected in this equation.

The NS equations (equations 2.1 and 2.2) build the foundation of fluid dynamics as they fully describe the flow, including all time and length scales. This leads to problems in some cases, where the range of scales is very large, e.g. in ABL simulations. The largest turbulent scales are in the order of the geometric boundary conditions and therefore around 10^3 m, while the smallest scales are about the size of the dissipative eddies, which is about 10^{-3} m [45]. To resolve all of these scales would require a massive amount of computer power, and thus it is infeasible. Moreover, in many cases in CFD it is not needed to resolve all scales, as only a part of them are in the field of interest. Sometimes one only needs to have information about the mean field and therefore does not need to resolve transient behavior at all. Thus, several approaches have been developed to make this kind of simulation feasible. The RANS simulation apply the Reynolds decomposition and time averaging to the NS equations and consequently reduce the computer time. LES apply spatial filters to the NS equations and therefore only resolve a part of the turbulent structures. Hence, they do provide transient solutions, but only calculate a certain spectrum of all turbulent scales.

2.2.3 Reynolds-Averaged Navier-Stokes (RANS) Equations

For the derivation of the RANS equations one needs to perform a Reynolds decomposition. This splits the variables into a time-averaged component and a fluctuating component. After that the equation needs to be time-averaged to get to the final RANS formulation. One wants to point out, that although the equations is time-averaged, the transient term of the NS-equations can be retained. This approach is called unsteady RANS (URANS) and is capable of resolving behavior on larger timescales than the averaging time [11]. However, since in this thesis only

[1] The Einstein summation notation is a convention, which implies summation over an indexed term in a formula. If an index appears twice in a single term it implies the summation over all values of that index.

the time-averaged RANS equations are used, the derivation of the RANS equations without retaining the transient term is done. A variable v is decomposed into the time-averaged value, denoted by $\bar{v}$, and the fluctuation value, denoted by v'. The decomposition now can be written as

$$v = \bar{v} + v'. \tag{2.3}$$

By applying this decomposition to the NS equations and conducting time-averaging, the final incompressible RANS equations are obtained. Additionally a steady mean flow is assumed [11]. The continuity equation is written as

$$\rho \frac{\partial \bar{v}_i}{\partial x_i} = 0. \tag{2.4}$$

The time-averaged momentum equations reads

$$\rho \frac{\partial \bar{v}_i \, \bar{v}_j}{\partial x_j} = -\frac{\partial \bar{p}}{\partial x_i} + \frac{\partial}{\partial x_j} \left(\mu \frac{\partial \bar{v}_i}{\partial x_j} - \rho \overline{v_i' v_j'} \right) \tag{2.5}$$

An important difference between the time-dependent NS equations and the (time-averaged) RANS equations is the new term, the so called Reynolds stress tensor $\tau_{ij} = \rho \overline{v_i' v_j'}$. This term is an important part of turbulence modeling and therefore a few characteristics are explained here. The tensor consists of the correlations between the different fluctuating velocities. The diagonal components represent the normal stresses, whereas the off-diagonal quantities represent the shear stresses. The basic structure of the tensor is shown in equation 2.6. It reads

$$\tau_{ij} = \rho \, \overline{v_i' v_j'} = \rho \begin{pmatrix} \overline{u'^2} & \overline{u'v'} & \overline{u'w'} \\ \overline{v'u'} & \overline{v'^2} & \overline{v'w'} \\ \overline{w'u'} & \overline{w'v'} & \overline{w'^2} \end{pmatrix}. \tag{2.6}$$

One can see, that the tensor is symmetric and therefore $\overline{u'v'} = \overline{v'u'}$, $\overline{u'w'} = \overline{w'u'}$ and $\overline{v'w'} = \overline{w'v'}$. In general the tensor represents an additional viscosity by introducing an additional stress term due to turbulent fluid motions. Additionally the Reynolds stress tensor is an unknown quantity. It introduces six new variables to the RANS equations. For the whole RANS equations there are now ten unknown variables, consisting of three velocity components, the pressure and the six Reynolds stresses. This is called a closure problem, because there are more unknown variables than number of equations. Thus several models have been developed to close the RANS equations and the main difference between these models is the way they resolve the Reynolds stresses [11][39].

2.2.4 Spatial Filtered Navier-Stokes Equations

Another approach used in the present study is the Large Eddy Simulation (LES). The main idea is to resolve the large energy-carrying eddies and to model the smaller scales. These eddies are expected to behave more homogeneous and isotropic according to the Kolmogorov theory, which is explained later in this section. Therefore, modeling is easier and closer to reality. Furthermore, the smaller the eddies the less

they depend on the boundary conditions of the domain. Hence, it is easier to create universal valid models, which can be used in different applications. Compared to Direct Numerical Simulation, known as the most expensive CFD method, in LES, the mesh can be coarsened, because only larger eddies need to be captured. This makes the LES approach significantly less resource demanding than DNS [26][49].

In order to receive the governing equations for LES, one needs to filter the physical quantities in the NS equations. Therefore, LES resolve transient behavior and these filtered variables are dependent on time and space. Similar to the Reynolds decomposition, a variable v is then written as

$$v = \tilde{v} + v'', \tag{2.7}$$

where $\tilde{v}$ denotes a spatial filtered variable and v'' denotes the subgrid-scale (SGS) component. Applying the filtering to the NS equations yields to the incompressible spatial filtered equations used for LES [26]. These equations have the same form as the initial NS equations. The spatial filtered continuity equation reads

$$\rho \frac{\partial \tilde{v}_i}{\partial x_i} = 0, \tag{2.8}$$

while spatial filtered the momentum equation reads

$$\frac{\partial \tilde{v}_i}{\partial t} + \frac{\partial (\tilde{v}_i \tilde{v}_j)}{\partial x_j} = -\frac{1}{\rho}\frac{\partial \tilde{p}}{\partial x_i} + \frac{\partial}{\partial x_j}(-\widetilde{\tau_{ij}} + 2\nu \tilde{D}_{ij}). \tag{2.9}$$

ν denotes the kinematic viscosity [26]. Note that $\tilde{D}_{ij}$ is the so called grid-scale rate-of-strain tensor, which is defined as

$$\tilde{D}_{ij} = \frac{1}{2}\left(\frac{\partial \tilde{v}_i}{\partial x_j} + \frac{\partial \tilde{v}_j}{\partial x_i}\right). \tag{2.10}$$

The SGS stresses are given by

$$\widetilde{\tau_{ij}} = \widetilde{v_i v_j} - \tilde{v}_i \tilde{v}_j. \tag{2.11}$$

Note that $\widetilde{\tau_{ij}}$ is used, to distinguish between the Reynolds stress tensor. To be precise it is incorrect to denote $\widetilde{\tau_{ij}}$ as a stress, since it is not multiplied by ρ and therefore has the wrong dimension [11]. However, it is often referred as stress and one will also refer to it as a stress in this study.

An important part of every LES is the type of filter that is used. The filter defines which range of scales is resolved and which is modeled. Therefore, has a direct impact on the need of computer resources.
A very common filter is the so called box filter, which is always used in finite volume method [11]. With the box filter the specific variable is averaged over the entire interval, or, in the case of a volume, over all dimensions. In the present study the filter size equals the computational grid. Thus, all scales that are captured depend on the grid size. Moreover, one can denote the scales, which are not resolved with a certain grid as subgrid-scales. The SGS stresses then represent the impact of the

unresolved small scale structures on the larger resolved structures. As introduced in equation 2.11, these stresses are unknown and need to be modeled, very similar to the previous presented RANS approach [11][26].

How much of all the scales should be captured can be derived from the energy density spectrum, which is shown in figure 2.6. While turbulence in general contains a wide range of different time and length scales, certain structures can be distinguished. Looking at figure 2.6, one can see three different parts. First, there are the large, energy-carrying scales, denoted by I. Second, there is the inertial subrange, labeled with II. This is also called Kolmogorov $-5/3$-range, which is discussed down below. Finally, the third part is the dissipation subrange, denoted by III [11].

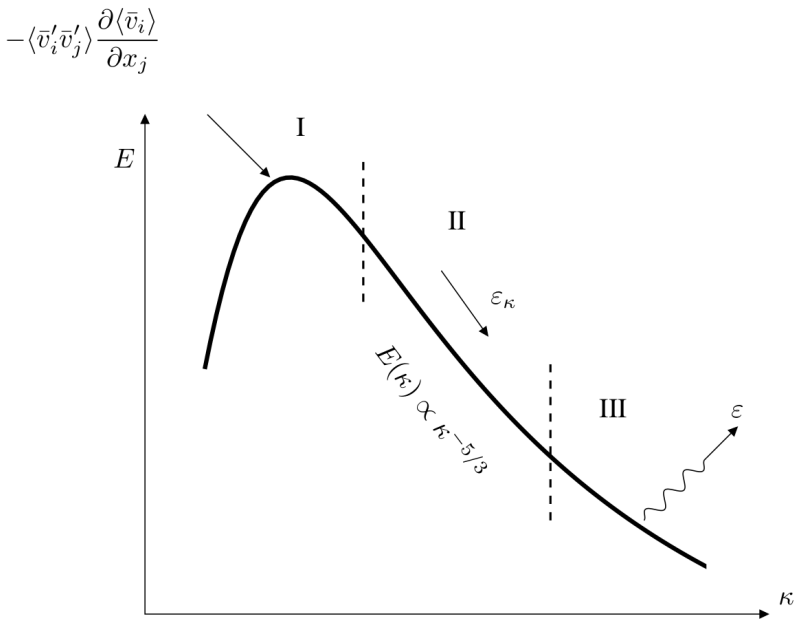

Figure 2.6: The energy density spectrum of turbulent kinetic energy. Figure taken from [11]

The different scales and the interactions between them are described by the so called energy cascade. In section I of the spectrum, the large eddies (and turbulence itself) are generated. This is denoted by the production term $-\left\langle \bar{v}_i' \bar{v}_j' \right\rangle \frac{\partial \langle \bar{v}_i \rangle}{\partial x_j}$ above the ordinate, which is discussed in section 2.2.5. The direction of motion is most likely dictated by outer conditions, i.e. the mean flow direction. Therefore, these eddies are highly anisotropic. These large eddies then transfer their energy to smaller eddies due to vortex stretching and velocity gradients. The eddies get smaller and at the same time less depending on outer parameters. Hence, at some point the eddies become isotropic. During this process the eddies also lose their kinetic energy and in relation to that viscous forces get stronger. Finally, in section III of the energy cascade, viscous forces are now strong enough to dissipate the eddies into heat energy, denoted by ϵ. This terminates the energy cascade as at some point small eddies can no longer exist due to viscous effects [11]. Kolmogorov first described the

size of these dissipative eddies with the so-called Kolmogorov length

$$\eta = \left(\frac{\nu^3}{\epsilon}\right)^{1/4}. \tag{2.12}$$

As equation 2.12 shows, this part of the spectrum only depends on the turbulent dissipation ϵ and the kinematic viscosity ν.

Between these two scales one finds the inertial subrange (II), which is only influenced by the cascade process itself [4]. To exist this region requires a sufficient high Reynolds number, so that the flow is fully turbulent. Eddies in this region are in the mid-range. Also the turbulence is isotropic, just like region III. Looking at the whole energy cascade this region is responsible for the spectral transfer. In this region one can also find the so called cut-off, which separates the resolved structures from the SGS stresses [11].

The inertial subrange is also called the Kolmogorov $-5/3$-range. This is because the decay of the energy spectra in this region is described by the following law, first presented by Kolmogorov [11]:

$$E(\kappa) = C_K \epsilon^{\frac{2}{3}} \kappa_w^{-\frac{5}{3}} \tag{2.13}$$

In this equation C_K represents the Kolmogorov constant, which is about $C_K = 1.5$ and κ_w is the wavenumber. One also wants to refer to the Kolmogorov hypothesis, where Kolmogorov pointed out the characteristics stated in this section [28][29].

2.2.5 Turbulence Modeling

In the previous sections 2.2.3 and 2.2.4 one introduced the basic principles and governing equations of the CFD methods used in the present study. Moreover, one presented the unknown term in RANS equations, called the Reynolds stress tensor, or, in case of the spatial filtered equations, the SGS stresses. Finally, one discussed the energy density spectrum of turbulence, explaining the different turbulent scales, behaviour and interactions. These discussions represent the physical point of view. In contrast to that, one presents the modeling approaches for these physical characterstics in this section.

Turbulence Modeling in RANS

First, turbulence models for the RANS approaches is investigated. Therefore, one can distinguish between different models based on the way they deal with the Reynolds stress tensor. The first approach is to model the unknown term τ_{ij} and therefore make some kind of assumption. In most cases this is the Boussinesq assumption. These approaches are generally known as models of first order. The second option is to solve the respective transport equation for the Reynolds stresses. This leads to six additional differential equations. Here it is not necessary to use the Boussinesq assumption, since the Reynolds stresses are actually calculated and not modeled. This is commonly known as models of second order such as the Reynolds

Stress Models (i.e. the Algebraic Stress Model). This can produce better resolved turbulence structure and therefore more accuracy in the solution. On the downside more equations have to be solved, more terms modeled and the computer power needed can increase. However, in the present study only models of first order are used which is why they are going to be in the focus here [11][39].

The models of first order can be distinguished even further by the number of differential equations needed to solve the problem. First, there are models using algebraic relations to describe the Reynolds stresses. Thus, they do not need more differential equations and therefore these models are called zero-equations-models, e.g. the mixing length model. Second, there are one-equation-models, introducing only one more differential equation into the problem. A very popular one-equation-model is the Spalart-Allmaras model [43]. Third and one of the most commonly used methods are the two-equation-models. Very popular two-equation-models are the k-ϵ model and the k-ω model and also various modifications of these two [49]. A fundamentally different approach is the LES, which was introduced in section 2.2.4. Finally, the DNS do not use any turbulence modeling at all, since every scale is resolved. An overview over the most common methods for turbulence modeling is shown in figure 2.7.

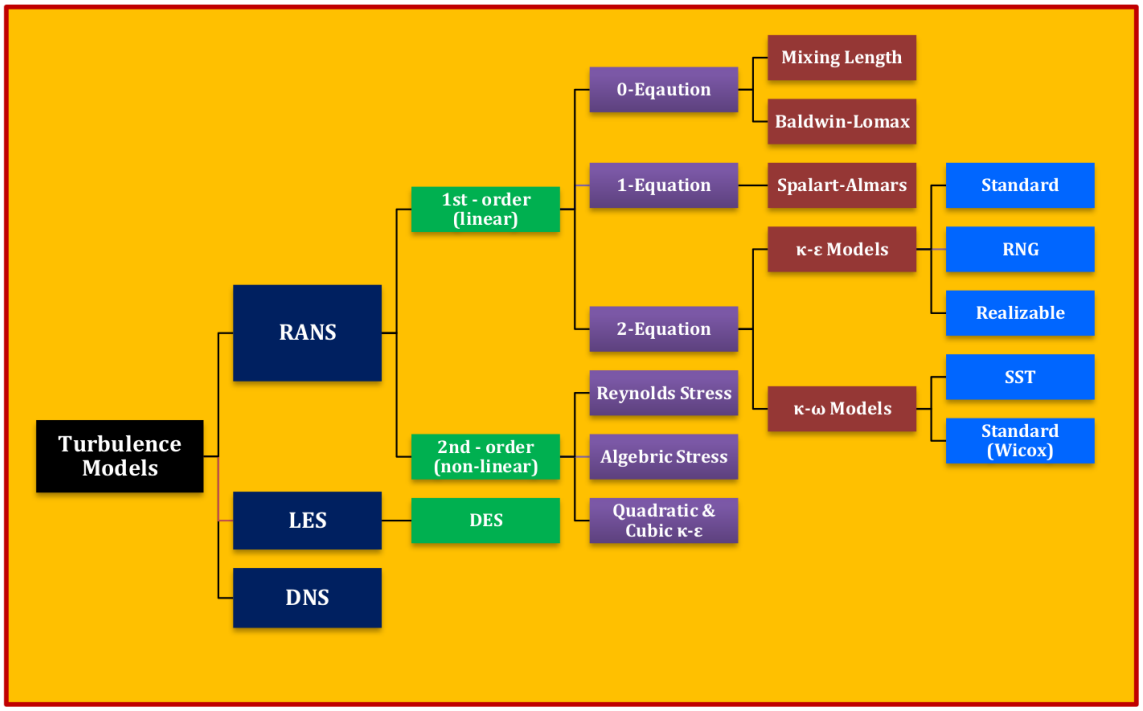

Figure 2.7: Overview over commonly used turbulence models. Figure adapted from [39]

In the following one gives a brief discussion of the different turbulence models and the general process of turbulence modeling. Therefore, the modeling of the Reynolds stresses of the respective approach are assessed. Most of the turbulence models use the Boussinesq assumption. Boussinesq proposed the idea, that Reynolds stresses behave proportional to the mean strain [39]. The basic idea is to replace the unknown

Reynolds stresses τ_{ij} with a turbulent viscosity ν_t. For the stress tensor one can now write

$$\overline{v_i' v_j'} = -\nu_t \left(\frac{\partial \bar{v}_i}{\partial x_j} + \frac{\partial \bar{v}_j}{\partial x_i} \right) + \frac{1}{3}\delta_{ij}\overline{v_i' v_i'} = -2\nu_t \bar{s}_{ij} + \frac{2}{3}\delta_{ij}k. \tag{2.14}$$

This means, that the six unknown Reynolds stresses are replaced by only one new unknown variable, the turbulent viscosity ν_t (also known as eddy viscosity). This viscosity is fundamentally different than a molecular viscosity, since it is not dependent on the fluid nor temperature, but only on the location [11]. Moreover, δ_{ij} denotes the Kroenecker's δ, which is defined as

$$\delta_{ij} = \begin{cases} 1 & i = j \\ 0 & i \neq j \end{cases}. \tag{2.15}$$

This makes sure, that the normal components of the stresses are allocated one equal third each and each Reynolds stress influences the equations in an isotropic manner [11]. Note that the Boussinesq assumption introduces a vast simplification.

The turbulent viscosity now needs to be calculated. It is defined as

$$\nu_t = u_t l. \tag{2.16}$$

u_t represents the turbulent velocity and l the turbulent length scale [39]. The turbulent velocity describes the typical velocity within the energy containing eddies while the turbulent length scale describes a typical length for these eddies. How to calculate these variables determines the respective turbulence model.

The one-equation models introduce one additional differential equation to determine the turbulent viscosity. In the beginnings, often the transport equation for the turbulent kinetic energy k was used [26]. This equation is derived from the NS-equation [11]. Because its importance for understanding turbulence phenomena like the energy density spectrum, the different terms of the equations are discussed here. For an incompressible flow with constant viscosity the transport equation reads

$$\underbrace{\frac{\partial \bar{v}_j k}{\partial x_j}}_{I} = \underbrace{-\overline{v_i' v_j'}\frac{\partial \bar{v}_i}{\partial x_j}}_{II} \underbrace{-\frac{\partial}{\partial x_j}\left[\frac{1}{\rho}\overline{v_j' p'} + \frac{1}{2}\overline{v_j' v_i' v_i'} - \nu\frac{\partial k}{\partial x_j}\right]}_{III} \underbrace{-\nu\overline{\frac{\partial v_i'}{\partial x_j}\frac{\partial v_i'}{\partial x_j}}}_{IV}. \tag{2.17}$$

In this equation term I represents the convection term. Term II describes the production of the turbulent kinetic energy. Including the minus sign it is always positive, presenting the energy that the turbulence extracts from the mean flow. The turbulent diffusion is represented by term III. One can distinguish between the pressure-, velocity fluctuation- and molecular diffusion. Finally term IV includes the turbulent dissipation ϵ into the equation. In contrast to the production term, it is always positive, excluding the minus sign. Therefore, it represents the conversion of the turbulent kinetic energy to thermal energy, especially taking place at smaller scales [10].

However, to actually make use of this equation a number of unknown quantities need to be determined. Using the Boussinesq assumption for the production term II the Reynolds stresses can be substituted [10]. This leads to

$$P_k = \nu_t \left(\frac{\partial \bar{v}_i}{\partial x_j} + \frac{\partial \bar{v}_j}{\partial x_i} \right) \frac{\partial \bar{v}_i}{\partial x_j}. \tag{2.18}$$

Next the diffusion term needs to be determined. Therefore the triple correlation is modeled by a gradient law. It is assumed that k is diffused from regions with higher k to a region with lower k, very similar to the transport of heat [10]. One can substitute the correlation as

$$\frac{1}{2}\overline{v_j v_i v_i} = -\frac{\nu_t}{\sigma_t} \frac{\partial k}{\partial x_j}. \tag{2.19}$$

σ_t denotes the turbulent Prandtl number [11]. It is defined as

$$\sigma_t = \frac{\nu_t}{\alpha_t}. \tag{2.20}$$

It represents the relation of the turbulent viscosity to the turbulent thermal diffusion α_t. With DNS and experimental results it is often determined that $0.7 \leq \sigma_t \leq 0.9$ [11]. The diffusion due to pressure is very small and therefore neglected [10]. Lastly the turbulent dissipation term is changed to

$$\epsilon = \frac{k^{\frac{3}{2}}}{l}. \tag{2.21}$$

The final modelled k equation now reads

$$\frac{\partial \bar{v}_j k}{\partial x_j} = P_k + \frac{\partial}{\partial x_j} \left(\left(\nu + \frac{\nu_t}{\sigma_t} \right) \frac{\partial k}{\partial x_j} \right) - \epsilon, \tag{2.22}$$

For convenience one refers to this equation as the transport equation for k. This equation is used to in the one-equation- and some of the two-equation-models as well [11].
Similar to the zero-equation-models, the turbulent length is needed here as well. This is why the original one-equation models did not make major improvements to turbulence modeling [10]. A more promising approach was presented with the Spalart-Allmaras model, which uses a transport equation for the eddy viscosity instead [26][43].

However, the most popular RANS turbulence models are the two-equations-models, especially the k-ω and the k-ϵ model. Since the latter of these two is used in this thesis one concentrates on that one.
When using the k-ϵ model one calculates the eddy viscosity with replacing the characteristic length and velocity with

$$\nu_t = c_\mu \frac{k^2}{\epsilon}, \tag{2.23}$$

where c_μ is one of the model constants [11]. The modelled transport equation for k has been derived above, now the modelled ϵ equation is presented [10]. Although the exact transport equation for ϵ can be derived from the NS-equations, the number of unknown variables and terms would be very large and therefore it is inconvenient to use. Thus, the transport equation often used for modelling is based on physical reasoning. It reads

$$\frac{\partial \bar{v}_j \epsilon}{\partial x_j} = \frac{\partial}{\partial x_j}\left(\left(\nu + \frac{\nu_t}{\sigma_\epsilon}\right)\frac{\partial \epsilon}{\partial x_j}\right) + \frac{\epsilon}{k}(c_{\epsilon 1} P_k - c_{\epsilon 2}\epsilon). \tag{2.24}$$

For solving all relevant equations in total five variables now have to be determined. While there can be found certain relations for three of these variables (c_μ, $c_{\epsilon 1}$, $c_{\epsilon 2}$), the two remaining variables(σ_k and σ_ϵ) can be optimized according to the certain flow, e.g. channel flow, pipes or jets etc. The standard values are shown in table 2.1 down below.

Table 2.1: Typical model constants for the k-ϵ model [10]

c_μ	$c_{\epsilon 1}$	$c_{\epsilon 2}$	σ_k	σ_ϵ
0.09	1.44	1.92	1.0	1.31

Since the k-ϵ model is widely used in the industry, a lot of effort has been put in optimizing its performance. When using the wall law, one can significantly reduce the number of grid points and therefore save computational time and costs. Furthermore, the model constants have been investigated in many applications and experiments providing a good accuracy for many cases. Lastly, the eddy viscosity is always positive. Thus, the numerical stability is very good [26].
However, there are cases, where the k-ϵ model does not provide accurate results. In general it performs poorly, when the eddy-viscosity assumption (Boussinesq) is not valid. Moreover, it has its difficulties, if the anisotropic Reynolds stresses gain in influence, since due to the Boussinesq assumption only the isotropic stresses are taken into account. Flows, which are not in local equilibrium might be resolved poorly as well, because $P_k \not\approx \epsilon$. Lastly, the k-ϵ model might has difficulties with flows, where the approximation k/ϵ and $k^{3/2}/\epsilon$ does not fit time and length scales. In general flows which large acceleration or deceleration, strong swirl or strongly curved streamlines are difficult to resolve correctly with the eddy viscosity approaches, like the k-ϵ model [49].

However, the k-ϵ model in its original form is typically not in use anymore. To address its weaknesses stated above, several advanced models have been developed. One of them is the Shear Stress Transport (SST) model, proposed by Menter [32]. It combines the strengths of the k-ϵ and k-ω model by applying the a blending function. Near the wall the k-ω model is used and moving into the free flow the k-ϵ model is applied. This leads to improvements especially for zero pressure gradient, and adverse pressure gradient boundary layers and free shear layers [49].

Another important variation is the realizable k-ϵ model, which is a non-linear model. This variation is also used in the present study. It modifies the anisotropic part of the Reynolds stresses without introducing the additional transport equation, like the turbulence models of second order (Reynolds stress models) do it. Moreover, the approximation of the eddy viscosity is changed as well. Thus, the realizable model considers the relaxation time, the turbulence needs to adjust itself to the flow domain. The Reynolds stresses now depend partially on the mean strain rate. This is a major improvement to the standard k-ϵ model, which is unable to reproduce physical flow structures, which change very quickly in the domain. While in the original k-ϵ model it is assumed that $P_k \approx \epsilon$ at all times, in the realizable k-ϵ model the turbulence is allowed to adjust itself and disturb this balance. This leads to better performance for instantaneous changes in the domain [39].

Turbulence Modeling using LES

Very similar to the RANS approach, the respective LES models can be distinguished from their modelling of the SGS stresses (equation 2.11). The most common approaches are discussed in this section. First one substitutes the SGS stresses with an eddy viscosity approximation, similar to a physical viscosity or the previous presented turbulent viscosity [26]. It yields

$$\widetilde{\tau_{ij}} = -2\nu_e \tilde{D}_{ij}. \tag{2.25}$$

ν_e is denoted as the SGS eddy viscosity coefficient [26]. One now substitutes the SGS stress tensor in equation 2.9 with equation 2.25. The momentum equation then reads

$$\frac{\partial \tilde{v}_i}{\partial t} + \frac{\partial(\tilde{v}_i \tilde{v}_j)}{\partial x_j} = -\frac{1}{\rho}\frac{\partial \tilde{p}}{\partial x_i} + \frac{\partial}{\partial x_j}\left[2(\nu + \nu_e)\tilde{D}_{ij}\right]. \tag{2.26}$$

Solving the filtered continuity and momentum equation (2.8 and 2.9) and providing the SGS eddy viscosity coefficient ν_e builds the basis for one of the most commonly used models, the Smagorinsky model [26]. For the eddy viscosity one can substitute

$$\nu_e = (C_s \Delta)^2 |\tilde{D}|, \tag{2.27}$$

where Δ denotes the filter width, C_s is called the Smagorinsky constant and $|\tilde{D}|$ represents the norm of the rate-of-strain tensor

$$|\tilde{D}| = \sqrt{2\tilde{D}_{ij}\tilde{D}_{ij}}. \tag{2.28}$$

The Smagorinsky constant is the only non-dimensional constant that needs to be given for this model. With the assumption of local equilibrium and the Kolmogorov spectra one finds the theoretical value $C_s = 0.173$ [26].

In general the Smagorinsky model provides good results for the energy dissipation under the condition of an appropriate Smagorinsky constant. It matches experimental results well, particularly for isotropic turbulence. Nevertheless, the Smagorinsky constant needs to be adapted for each scenario. Hence, it is not universal. Moreover,

it does not perform well on predicting the turbulent behaviour in the subgrid scales. Accurate data with DNS showed, that the modelled SGS stresses differ from the actual SGS stresses obtained by these simulations. Furthermore, the Smagorinsky model can only transfer energy from larger to smaller eddies, because ν_e is always positive. Thus, it cannot reproduce the inverse cascade (backward scatter), which can exist in reality. For practical use the high robustness of the Smagorinsky model is a very important factor [26][49].

To address the downsides of the standard Smagorinsky model, different variations have been developed. One of the most commonly used approaches are the dynamic models. These methods use the local grid-scale turbulence mechanism additionally to the grid-scale velocity gradients to resolve the SGS eddy viscosity. In the standard Smagorinsky model the constant C_s was chosen invariable. In the dynamic approaches C_s changes dynamically depending on the grid-scale velocity field. This approach is known as the dynamic Smagorinsky model (DSM) [26].
Major improvements of the DSM are treatment of laminar to turbulent transition, the treatment near the wall and the inverse energy cascade, which is now possible within the model. However, the DSM suffers from numerical instability [26].

Besides the RANS and LES approaches the so called hybrid LES/RANS method is also a promising approach. This method combines RANS and LES by treating the near wall flow with the URANS approach and the free flow as the LES. The main justification for these models is the reduction of cells, especially in near wall regions. In standard LES, the grid near the walls must be very fine in order to capture the physics. This is because the scales of the turbulent eddies are very small next to the wall and getting even smaller for larger Reynolds numbers. in hybrid approaches, RANS wall functions are applied in that regions, so that the mesh can be coarsened. In the outer regions LES is used [11].

2.2.6 Modeling of the Atmospheric Boundary Layer

The modeling of the ABL is a complex task. There is a huge variety of scales and the computational domain often needs to be very large. In order to describe the physical quantities in the ABL, different approaches were developed. In the present study one focuses on the modeling approaches for the neutral ABL. A commonly used method for ABL modeling with the k-ϵ model was introduced by Richard and Hoxey [38] and is often referred to as the logarithmic law. The logarithmic law is derived with physical and dimensional considerations. Among others, the Prandtl mixing length is used (very similar to the zero-equation turbulence models). One obtains an equation for the vertical gradient of the wind speed. Finally, with the integration one derives the mean velocity distribution [13][50]. It reads

$$u(y) = \frac{u_*}{\kappa} \ln \frac{y_0 + y}{y_0}. \tag{2.29}$$

y_0 denotes the roughness length, which depends on the surface characteristics and y is the distance perpendicular to the surface. For offshore environment the value is

very small, because the surface is very smooth [47]. Moreover, κ represents the von Kármán constant. Finally, u_* is the so called friction velocity. It is defined as

$$u_* = \frac{\kappa u_{\text{ref}}}{\ln \frac{y_0 + y_{\text{ref}}}{y_0}} \tag{2.30}$$

with the reference velocity u_{ref} at the reference height y_{ref}. Furthermore, to complete the boundary conditions for ABL modeling, the turbulent quantities need to be defined. The turbulent kinetic energy reads

$$k = \frac{u_*^2}{\sqrt{c_\mu}}, \tag{2.31}$$

while the equation for the turbulent dissipation yields

$$\epsilon = \frac{u_*^3}{\kappa(y_0 + y)}, \tag{2.32}$$

with the model constant c_μ. These boundary conditions fit the k-ϵ turbulence model, meaning they fulfill the transport equation for k and for ϵ.

2.2.7 Turbulent Quantities

Finally, the physical quantities, that have not been introduced yet are discussed in this section. First and foremost the Reynolds number, as it is one of the most important non-dimensional parameters for viscous flows. It describes the ratio between the inertial and the viscous term and is defined as

$$Re = \frac{UL}{\nu}. \tag{2.33}$$

U and L describe the characterstic velocity and length, respectively [26]. These are characteristic values for each flow domain. In the present study one assumes the characteristic velocity to be 10 $\frac{\text{m}}{\text{s}}$ and the characteristic length to be 1000 m, as this is the height of the Ekman sublayer investigated in this study. One calculates the approximate Reynolds number for the present study as

$$Re = \frac{10 \ \frac{m}{s} \cdot 1000 \ m}{1.45 \cdot 10^{-5} \ \frac{m^2}{s}} = 6.9 \cdot 10^8. \tag{2.34}$$

The kinematic viscosity was calculated for an altitude of 90 m and a temperature of 287.565 K [52]. The flow over a flat plate is considered to be fully turbulent above Reynolds numbers of $Re_L = 5 \cdot 10^5$ (where L is the distance from the leading edge) [20]. Therefore, the flow investigated in the present study is fully turbulent [49].

Besides the impact of the Reynolds number on the physical behaviour of the flow, it has also a large influence on the CFD simulations. The larger the Reynolds number is, the wider the range of length scales gets in turbulent flows. Therefore, resolving all scales in high Reynolds number flows becomes infeasible at some point. This is one of the major justifications for the use of turbulence models [26].

Moreover, the energy referred to the velocity fluctuations is quantified by the turbulent kinetic energy k. It reads

$$k = \frac{1}{2}\overline{v_i' v_i'} = \frac{1}{2}(Re_{xx} + Re_{yy} + Re_{zz}), \tag{2.35}$$

where Re_{xx}, Re_{yy} and Re_{zz} denote the normal components of the Reynolds stresses [51]. They can be calculated according to

$$Re_{ii} = \overline{v_i'^2}, \tag{2.36}$$

as they equal the variances of the turbulent velocity fluctuations, with $i = 1, 2, 3$ for the streamwise, wall-normal and spanwise direction, respectively.

Finally, one introduces the turbulence intensity I in the respective direction. It is defined as

$$I_i = \frac{\sqrt{\overline{v_i'^2}}}{\bar{v}_i}. \tag{2.37}$$

It represents the turbulent fluctuations with regard to the mean velocity [51]. The turbulence intensity is often needed to set the boundary conditions of the CFD calculation, but also for the physics of wind turbines. The higher the turbulent fluctuations the higher the induced stresses on the turbine. Therefore, it is important to predict the turbulence intensity.

2.3 Wind Turbine Aerodynamics and Loads

In this section the basic principals of wind turbine rotor aerodynamics are discussed. Furthermore, one introduces the Actuator Disk momentum theory, which builds the foundation for the Actuator Disk Model (ADM). Moreover, one presents the blade element method and combines these two approaches to the Blade-Element-Momentum (BEM) theory. The BEM theory is used within the Actuator Line Model (ALM) and together with the ADM both of these models are used within the commercial CFD solver *Star-CCM+* to simulate ABL and rotor aerodynamics. Finally, one presents the aero-elastic solver *FAST*.

2.3.1 Aerodynamic Characteristics

The main intention for using a wind turbine is to extract kinetic energy from a wind flow and transform it first to mechanical and then to electrical energy. Inevitably a force acting on the rotor blades is induced by the flow. For the assessment of these forces, one looks at the individual sections of the blade, which consist of different airfoils. The resulting force acting on an airfoil can be split into the force created by pressure (normal force) and the tangential component, which is called friction force. Furthermore, the forces are often divided into a component perpendicular to the flow direction (lift) and parallel to the flow (drag) [8].

Different coefficients describe these forces and aerodynamic behaviour of an airfoil. The lift coefficient is defined as

$$C_l = \frac{L}{\frac{1}{2}\rho V_0^2 c}, \tag{2.38}$$

where L denotes the lift force per span, ρ is the density, V_0 is the wind speed in the free stream and c is the chord length[2]. The lift coefficient is a function of the Reynolds number or Mach number and the angle of attack (AOA). However, the Reynolds number usually affects the state of the boundary layer and therefore the risk of flow separation, which is mainly important for the maximum lift coefficient. Higher Reynolds numbers lead to higher stall AOA and higher maximum lift coefficients. In the usual operating range, the influence of the AOA is much more important. Therefore, the lift coefficient is usually stated as a function of the AOA.

Another important aerodynamic characteristic is the airfoil drag, which is presented by the drag coefficient C_d. It is defined as

$$C_d = \frac{D}{\frac{1}{2}\rho V_0^2 c}, \tag{2.39}$$

where D denotes the drag force per span experienced by the airfoil. Similar to the lift coefficient the drag coefficient is often plotted against the AOA. However, it can also be shown as a function of the lift coefficient.

2.3.2 Actuator Disk Momentum Theory

In the following the Actuator Disk momentum theory is derived. The momentum theory is a simplified approach for assessing the momentum balance on a rotating stream tube. Therefore, it represents the actual turbine rotor as a circular disk, where friction is neglected [8][33]. This disk is extended both upstream and downstream, creating a stream tube as shown in figure 2.8.

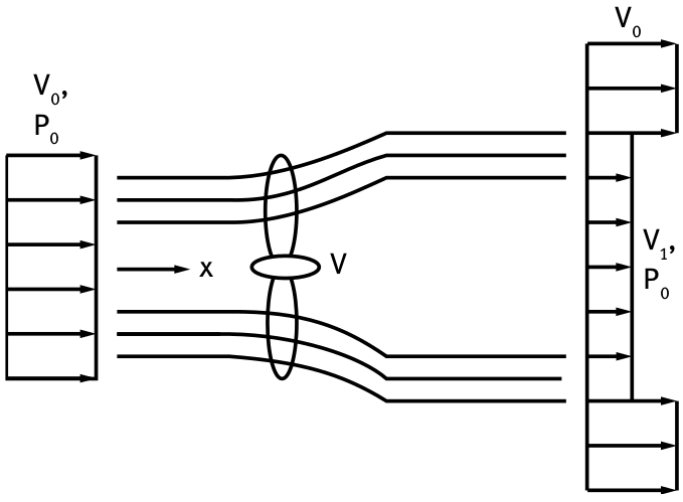

Figure 2.8: Illustration of the Actuator Disk model. Figure taken from [8]

[2]The chord length is the shortest distance between the trailing and leading edge of an airfoil.

The stream tube forms a control volume with cylindrical shaped ends, for which the momentum balance is assessed. There are four important sections of the stream tube. The first one is far upstream in the free stream region, two sections are right before and after the disk (rotor) and the last one is far downstream in the far wake region.

The flow enters the stream tube with the axial velocity V_0 and the pressure p_0, representing the free stream conditions. When passing the disk, the flow experiences a pressure drop Δp and a reduction of the axial velocity V as well, because kinetic energy is taken from the flow by the disk. When the flow leaves the stream tube it has the axial velocity V_1 and the pressure p_0. The axial velocity and static pressure as a function of the axial distance x is drawn in the figure 2.9.

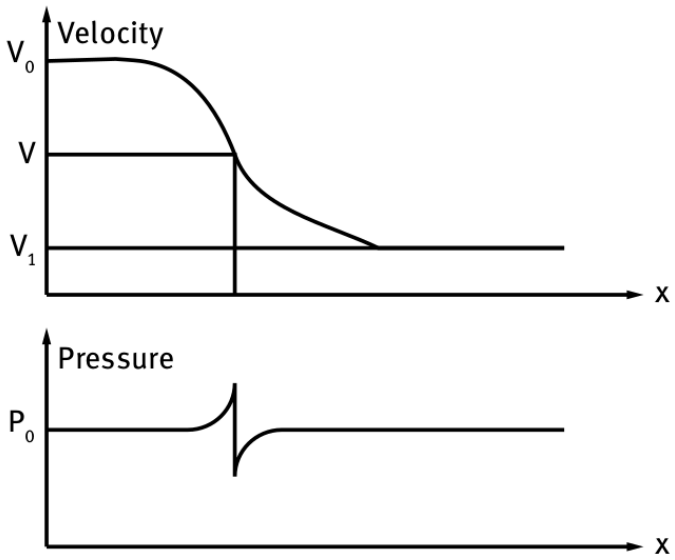

Figure 2.9: Axial velocity and static pressure curve of the flow over an Actuator Disk. Figure taken from [8]

One can see, that the velocity is reduced after the disk, but the pressure recovers to the free stream pressure p_0 in the far wake region. Another important characteristic is the velocity gradually decreasing before the flow reaches the turbine. This is due to the extraction of kinetic energy by the turbine. Additionally, the rotor induces a radial velocity because of the flow expanding upstream of the turbine. In contrast to that, the pressure increases slightly just in front of the rotor because of the stagnation of the velocity and therefore transformation from dynamic pressure to static pressure. Then a sudden pressure drop is caused by the disk, which can be explained by the basic momentum theory. After the disk the pressure recovers to the free stream pressure p_0 [8].

The governing equation of the Actuator Disk momentum theory are now derived on the basis of Chen et al. [8] and Schaffarczyk [41] and written in the way they are implemented in the CFD software *Star-CCM+* [1]. When applying the axial momentum theory to the control volume mentioned above, one can state two formulations

for the change in axial force (thrust), that reads

$$\mathrm{d}T = \mathrm{d}m(V_0 - V_1) = \rho V(V_0 - V_1)\mathrm{d}A, \tag{2.40}$$

and

$$\mathrm{d}T = \Delta p \mathrm{d}A, \tag{2.41}$$

where $\mathrm{d}m$ represents the mass flow rate in the control volume and $\mathrm{d}A$ represents the change of the section area of the stream tube. Assuming incompressible and steady flow allows the application of Bernoulli's law before the turbine and after the turbine. Because of the extraction of kinetic energy the total pressure decreases after the rotor. One obtains a relationship for the pressure drop Δp. It reads

$$\Delta p = \frac{1}{2}\rho(V_0^2 - V_1^2). \tag{2.42}$$

Combining equation 2.40, 2.41 and 2.42 yields

$$V = \frac{V_0 + V_1}{2}. \tag{2.43}$$

For convenience the axial induction factor a is introduced[3]. The equations for the velocities then read

$$V = V_0(1 - a) \quad \text{and} \quad V_1 = V_0(1 - 2a). \tag{2.44}$$

Inserting equation 2.44 into equation 2.40 gives

$$\mathrm{d}T = 4\pi\rho V_0^2 a(1 - a)r\mathrm{d}r. \tag{2.45}$$

Substituting the dimensionless thrust coefficient $C_t = 4(1 - a)a$ [41] gives another formulation, which reads

$$\mathrm{d}T = \frac{1}{2}\rho V_0^2 C_t 2\pi r\mathrm{d}r \tag{2.46}$$

or for the total thrust of the wind turbine

$$T = \frac{1}{2}\rho V_0^2 C_t \pi(r_{\mathrm{out}}^2 - r_{\mathrm{in}}^2), \tag{2.47}$$

where r_{out} and r_{in} denotes the outer and inner Radius of the disk, respectively. Although in theory the actuator disk is infinitesimally thin, the source therms are added for a actuator disk thickness δ. The thrust for a certain Δr annulus can be written as

$$\Delta T = \frac{1}{2}\rho V_0^2 C_t 2\pi r\Delta r. \tag{2.48}$$

[3]The axial induction factor a, sometimes also called axial interference factor, describes the velocity induced on the profile by the free stream. According to the Betz-Joukovsky theory the power and thrust coefficient depend on a. There are maximums of both coefficients, which is called the Betz-Jokouvsky limit [41].

Using equation 2.47 yields

$$\Delta T = T\frac{2r\Delta r}{r_{\text{out}}^2 - r_{\text{in}}^2}. \tag{2.49}$$

The thrust per per unit volume within a certain annulus then reads

$$\frac{\Delta T}{\Delta V} = \frac{T}{\delta\pi(r_{\text{out}}^2 - r_{\text{in}}^2)} = \frac{1}{2}\frac{\rho V_0^2 C_t}{\delta}, \tag{2.50}$$

with the unite volume of $\Delta V = 2\pi r\Delta r\delta$. For each cell that yields

$$T_{\text{cell}} = \frac{\Delta T}{\Delta V}V_{\text{cell}}. \tag{2.51}$$

Finally equation 2.51 needs to be scaled, in case the cell is not fully within in the disk. This leads to

$$T_{\text{cell}} = T\frac{V_{\text{cell}}}{\sum_{\text{allcells}} V_{\text{cell}}}. \tag{2.52}$$

A similar approach is used for the calculation of the torque distribution. The torque acting on an element for an annular ring with the width dr and the induction angular velocity ω is obtained with the conservation of angular momentum. It reads

$$\mathrm{d}Q = \mathrm{d}m(\omega r)r = 2\pi\rho V\omega r^3\mathrm{d}r. \tag{2.53}$$

Additionally to the axial induction factor a, the tangential induction factor b is defined as

$$b = \frac{\omega}{2\Omega}, \tag{2.54}$$

where Ω denotes the rotational rotor speed. Inserting the induction factors and integrating equation 2.53 leads to the total torque

$$Q = b(1-a)\frac{1}{2}\rho V_0\Omega\pi(r_{\text{out}}^4 - r_{\text{in}}^4). \tag{2.55}$$

The torque per unite volume is defined as

$$\frac{\Delta Q}{\Delta V} = \frac{2Wr^2}{\delta\pi(r_{\text{out}}^4 - r_{\text{in}}^4)}. \tag{2.56}$$

Similar to the thrust, the torque for each cell then reads

$$Q_{\text{cell}} = \frac{\Delta Q}{\Delta V}V_{\text{cell}} = \frac{2Qr_{\text{cell}}^2 V_{\text{cell}}}{\delta\pi(r_{\text{out}}^4 - r_{\text{in}}^4)}. \tag{2.57}$$

The final equation for the torque, with applied scaling yields

$$Q_{\text{cell}} = \frac{Qr_{\text{cell}}^2 V_{\text{cell}}}{\sum_{\text{allcells}} r_{\text{cell}}^2 V_{\text{cell}}}. \tag{2.58}$$

The tangential force for each cell is then defined as

$$F_{\text{tangential}} = \frac{Qr_{\text{cell}}V_{\text{cell}}}{\sum_{\text{allcells}} r_{\text{cell}}^2 V_{\text{cell}}}. \tag{2.59}$$

The thrust (axial force, equation 2.52) and the tangential force (equation 2.59) are now used to create the source term, which is added to the momentum equations [1].

2.3.3 Blade Element Method and Actuator Line Model

The blade element method is an approach to model rotor effects and especially to resolve the wake flow field without describing the exact geometry of the rotor blades. Body forces are modelled along lines, which are representing the blades [1][33].

Applying the blade element method is a two steps process. First, one needs to mark the cells that are used as a virtual disk and where the source term is added and second, the source term for the respective cell needs to be calculated [1].

The marking and allocation process is shown in figure 2.10. The red grid is the initial finite volume mesh, whereas the black grid is an interpolation grid. The marking takes place in two steps. In the first step, all cells in the volume mesh are marked, which are lying in the disk area. Then, each marked cell is assigned to an element of the interpolation grid and the location is stored with respect to the interpolation grid. One can see, that after these two steps all of the marked cells belong to one of the elements of the interpolation grid. This also means, that there has to be at least one cell in each element of the interpolation grid, which can cause problems especially in the inner area [1].

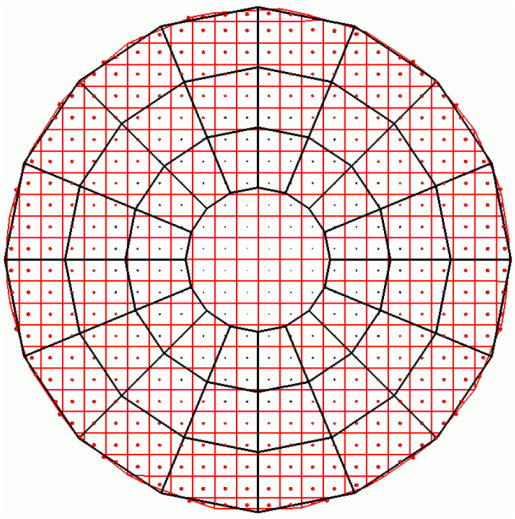

Figure 2.10: Cell marking within the blade element method. Figure taken from [1]

After marking the cells the source term is calculated for each element of the interpolation grid and afterwards transferred to the volume mesh. During this process

different coordinate transformations need to be conducted. Besides the global coordinate system of the whole domain, a local Cartesian coordinate system (i.e. x', y', z') is created in the center of the disk. The z'-direction is perpendicular to the disk, pointing in the thrust direction. Moreover, the disk rotates around the z' axis. In case of rotor blade flapping two additional coordinate systems are created, a cylindrical system with respect to the base of the local Cartesian coordinate system and a so called flap coordinate system, which is another Cartesian coordinate system with respect to the base of the previous created cylindrical coordinate system. This way the rotation of the disk and each blade is fully described[1].

All calculations are done within the flap coordinate system. Afterwards they are transformed to the global coordinate system and finally added to the momentum equations. For this the angle of attack and the relative velocity experienced by the blade is determined. Then, the lift and drag force is calculated according to

$$L = \frac{1}{2}\rho|v_{\text{rel}}|^2 C_l c \, \mathrm{d}r \tag{2.60}$$

and

$$D = \frac{1}{2}\rho|v_{\text{rel}}|^2 C_d c \, \mathrm{d}r, \tag{2.61}$$

where ρ, v_{rel} and c denote the density, relative velocity and chord length, respectively. The aerodynamic coefficients for lift and drag are denoted by C_l and C_d, respectively and $\mathrm{d}r$ represents the with of the individual element. For further improvement one can also add the tip-loss correction. However, since it was not used in the present study, it is not further explained here. Finally, the lift and drag force are transformed to the normal and tangential component [1]. It yields

$$F_{\text{norm}} = L\cos\beta - D\sin\beta \tag{2.62}$$

and

$$F_{\text{tang}} = L\sin\beta - D\cos\beta, \tag{2.63}$$

where β denotes the inflow angle. Now, the force vector is assembled and transformed into the global coordinate system. Before adding the force vector to the momentum equations, it is time-averaged over each blade element [1].

2.3.4 Blade-Element-Momentum (BEM) Theory

The BEM theory consists of the combination of two methods to assess the dynamic response of a turbine in a flow field. The Actuator Disk momentum theory is one approach and was introduced in section 2.3.2. The other one is the Blade Element theory, which assesses the aerodynamic loads on the blade at different sections. Together these two approaches provide four equations for the BEM method, which is then solved iteratively [8][21].

Two equations come from the momentum theory. The axial force (thrust) is defined as in equation 2.45, whereas the torque is given as

$$\mathrm{d}Q = 4b(1-a)\rho V_0 \Omega r^3 \pi \mathrm{d}r. \tag{2.64}$$

Note, that this formulation equals equation 2.55 in its differential form. Furthermore, the tip-loss correction is not considered here.

Additionally, the blade element theory delivers another two equations for the thrust and the torque, expressed by lift and drag coefficients. The thrust is defined as

$$\mathrm{d}T = \sigma\pi\rho\frac{V_0^2(1-a)^2}{\cos^2\beta}(C_l\sin\beta + C_d\cos\beta)r\mathrm{d}r, \tag{2.65}$$

whereas the equation for the torque reads

$$\mathrm{d}Q = \sigma\pi\rho\frac{V_0^2(1-a)^2}{\cos^2\beta}(C_l\cos\beta - C_d\sin\beta)r^2\mathrm{d}r. \tag{2.66}$$

Note that σ denotes the solidity

$$\sigma = \frac{Bc}{2\pi r}, \tag{2.67}$$

where B, c and r denote the number of blades, the chord length and the radius, respectively. These four equations (2.45, 2.64, 2.65 and 2.66) are now combined to receive the relationships

$$\frac{a}{1-a} = \frac{\sigma(C_l\sin\beta + C_d\cos\beta)}{4\cos^2\beta} \tag{2.68}$$

and

$$\frac{b}{1-b} = \frac{\sigma(C_l\cos\beta - C_d\sin\beta)}{4\lambda\cos^2\beta}, \tag{2.69}$$

where λ denotes the tip-speed ratio (TSR)

$$\lambda = \frac{\Omega r}{V_0}. \tag{2.70}$$

A typical iteration process goes as follows. To begin with the iteration, values for the induction factors a and b are guessed. By solving the equations 2.68 and 2.69 one calculates the inflow angel β and the TSR λ. The aerodynamic coefficients C_l and C_d are then determined using tabulated airfoil tables for the individual profile. This gives information about the aerodynamic performance of the turbine in this particular operating point. Finally, the induction factors are calculated again to start a new iteration [21].

Aero-Elastic Assessment

In the previous sections 2.3.2, 2.3.3 and 2.3.4 the theory used for the aero-elastic assessment was discussed. Within *Star-CCM+* the ADM and ALM are used to calculate turbine forces such as thrust and torque. Although the ALM and *FAST* both use the BEM theory to calculate the aerodynamic forces, there are various differences in the actual application. These are now discussed and it is outlined, why using *FAST* has several advantages.
First, the rotation rate is fixed in *Star-CCM+*. In contrast to that *FAST* has an included control system, adapting the rotation rate and other turbine characteristics to the current operating point. This is especially important when simulating complex or extreme situation, where the control system plays an important role. Furthermore, the effect of the tower and nacelle can be simulated in *FAST* but not in *Star-CCM+*. However, nowadays it is possible to model these effects within the ADM and ALM in general [44]. Finally, *FAST* works with an instantaneous field, while the ADM and ALM are mostly designed for a steady wind field.
In addition to that, *FAST* is a popular tool for assessing wind turbine loads and therefore it is well documented and provides reference cases and values for various applications.
FAST consists of different modules, which are briefly described here. As an input one needs to provide a flow field. This is transmitted through the *InflowWind* module to the *AeroDyn* module. Here the forces and moments are calculated according to the BEM theory. An additional module called *HydroDyn* is available to include wave loads for offshore applications. The resulting dynamic stresses for drivetrain, rotor, nacelle and tower are then determined within the *ElastoDyn* module. Similar to that the substructure is calculated in the *SubDyn* module. Finally, the *ServoDyn* module calculates power outputs.

2.4 Reference Turbine

For assessing the performance and accuracy of the conducted calculations in the present study one chose the *NREL offshore 5-MW baseline wind turbine* developed by the *National Renewable Energy Laboratory* (NREL) as a reference turbine. It is widely used as a standard reference for developing and improving concept studies for wind technology. The most important characteristics for this study are shown in table 2.2 according to the documentation from the NREL [23].

Table 2.2: Characteristics of the NREL offshore 5-MW baseline wind turbine [23]

Rating	5 MW
Rotor Orientation, Configuration	Upwind, 3 Blades
Control	Variable Speed, Collective Pitch
Rotor, Hub Diameter	126 m, 3 m
Hub Height	90 m
Cut-In, Rated, Cut-Out Wind Speed	3 m/s, 11.4 m/s, 25 m/s
Cut-In, Rated Rotor Speed	6.9 rpm, 12.1 rpm

The turbine was created as a conventional three-bladed upwind variable-speed and variable blade-pitch-to-feather-controlled turbine. In addition to the general characteristics the steady-state behaviour is documented as well. It is shown in figure 2.11.

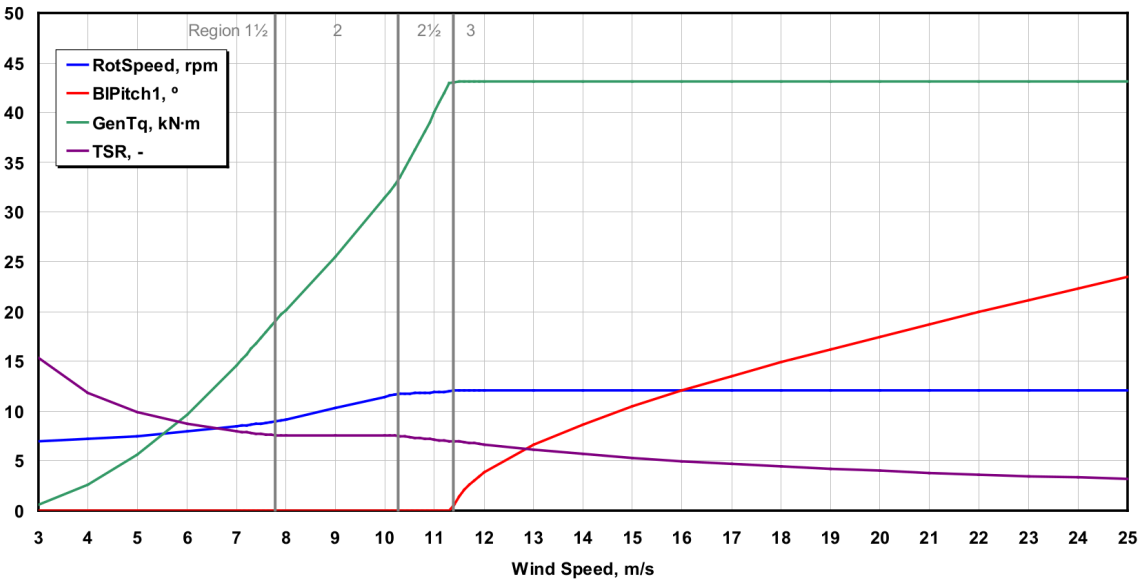

Figure 2.11: Steady-state behaviour of the NREL offshore 5-MW baseline wind turbine. Figure taken from [23]

One can see the operating range reaching from 3 m/s wind speed (cut-in) to 25 m/s (cut-out). Outside of this range the wind is either not strong enough to sufficiently generate power, or it is too strong so the stresses on the turbine would become too high. When looking at the green curve, one can see the generated torque, which is increasing quadratically with the wind speed until it reaches its maximum and held constant at the rated wind speed of 11.4 m/s. Then the active pitch control regulates the rotor speed, which is displayed by the red curve. Furthermore, one can see that the rotor speed is held constant at velocities higher than the rated velocity due to the pitch control. The TSR is constant in Region 2 to ensure a good efficiency of the wind to power transformation and gradually decreases afterwards, because the rotor speed is constant in that region.

3
Methods

This chapter describes the numerical methods used in the present project work. In the beginning, the computational domain is described, explaining the boundary conditions on the one hand and the computational discretization (the mesh) on the other. Furthermore, the simulation process is outlined.
In total four different types of Computational Fluid Dynamics (CFD) simulations were conducted. First of all, a Reynolds-Averaged Navier-Stokes (RANS) simulation was implemented to generate the correct inlet conditions for a superior Large Eddy Simulation (LES). This is necessary to provide a velocity profile and turbulent quantities in order to generate correct boundary conditions for the LES. After the validation of the LES the Actuator Disk Model (ADM) and Actuator Line Model (ALM) were implemented. The ADM and ALM provide additional outputs, e.g. power and thrust of the wind turbine, which will be assessed and compared with the *FAST* calculations. Moreover, they deliver information about the wake of each turbine.

Further on, the transient flow field generated with the LES was used for aeroelastic simulations with *FAST*. For comparison and validation another flow field was transmitted to *FAST*, which was created with the spectral method. These two simulations were investigated to outline differences between these models.

3.1 Computational Domain

For all simulations the computational domain is set up as a rectangular box. It is shown in figure 3.1. In the x-direction (streamwise) the domain extends 6000 m, in the z-direction (spanwise) it measures 4000 m and the height is 1000 m (y-direction, wall-normal). Two turbines are investigated in the present study. The center of each turbine (hub height) is at the location $[x, y, z] = [2000, 90, 2000]$ m and $[x, y, z] = [4000, 90, 2000]$ m, respectively. This distance is chosen that the wake of the first turbine does not affect the second. Several probes are placed at these locations and at upstream and downstream positions, pointing in y and z direction. This will be discussed together with the results in chapter 4.
The inlet surface is marked yellow, while the outlet region is coloured red. The bottom of the domain (gray) is set up as a flat plate, since the offshore environment is very smooth. The remaining three surfaces are symmetry planes. One discusses the boundary conditions of the individual simulations more in detail within the respective sections.

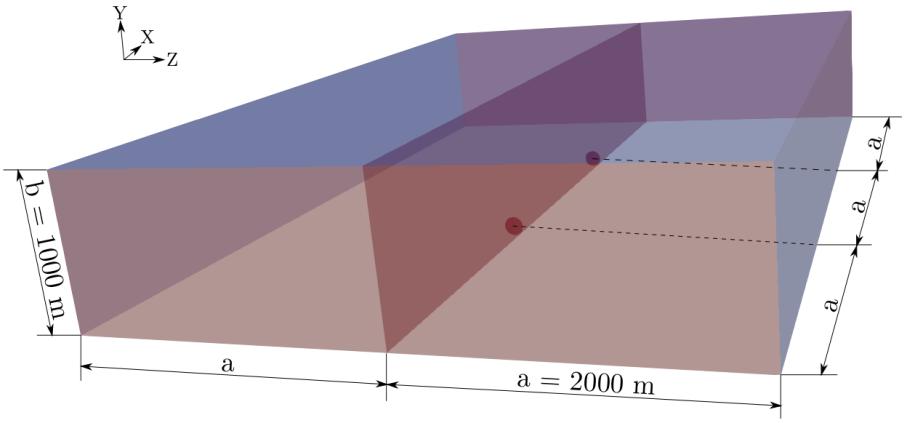

Figure 3.1: Computational Domain used for the CFD simulation in *Star-CCM+*

3.1.1 Mesh

Overall, two different meshes are used. For the RANS simulation and LES the *Trimmer* and *Prism Layer Mesher* are selected. The base size of the cells is set to 20 m in both cases. This is also the maximum cell size in the domain. Different base sizes were tested and 20 m proved to be the most efficient option while retaining good accuracy. To refine the near wall region, a prism layer is constructed next to the plate. There are 80 prism layers, building a refined region from the plate up to an altitude of 200 m. The first cell size is very important in Atmospheric Boundary Layer (ABL) modeling. The first layer of cells is about 0.004 m thick (in y-direction), which shows good agreement to the recommended cell size of the *Star-CCM+* user guide [1]. This leads to $y+$ values around 30. The total number of cells for the RANS simulation and LES is 7.2 million cells. Note that this mesh is not shown here due to its simplicity.

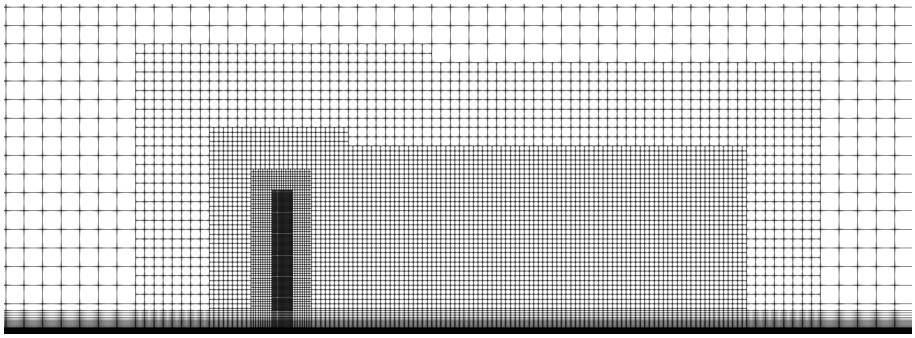

Figure 3.2: Sideview of the mesh for the Actuator Disk Model and Actuator Line Model

For the ADM and ALM approach the mesh is different, due to the requirements of these models. A cut through the y-z plane is shown in figure 3.2. The *Surface*

Remesher is added as an additional mesher. Most importantly the region around the actuator disks needs to be refined. That is why two *Volumetric Controls* are set up for each disk. The cells adjacent to the disk are very refined cubic cells, with a cell size of 1.25 m. The *Volume Growth Rate* is set to very slow for a smooth growth and appropriate cell quality. A second refined region is defined to have accurate results in the wake flow field. The cubic cells in this region measure 5 m in edge length. The prism layer is significantly reduced for the ADM and ALM approaches. Since *Volumetric Controls* starts at a height of $y = 25$ m, the total thickness of the prism layer equals this value. The total number of prism layers is 30 m and the first cell height is around 0.125 m, leading to $y+$ values around 1000. The total number of cells is around 6.5 million.

3.2 RANS Simulation

In this section one covers the setup of the conducted RANS simulation. As a turbulence model the realizable k-ϵ model is used. It is a steady, 3D simulation with a constant density. The initial conditions, reference values and fluid characteristics are defined as written in table 3.1. The density, viscosity and static pressure are chosen according to the standard atmospheric conditions at an altitude of 90 m (hub height) [52].

Table 3.1: Initial conditions, reference values and fluid characteristics for the RANS simulation

Type	Quantity	Value
Fluid characteristics	Density	$\rho = 1.21\ \frac{\text{kg}}{\text{m}^3}$
Fluid characteristics	Dynamic viscosity	$\mu = 1.89 \cdot 10^{-5}\ \frac{\text{kg}}{\text{ms}}$
Reference Value	Pressure	$p = 1 \cdot 10^5\ \frac{\text{kg}}{\text{ms}^2}$
Initial condition	Pressure	$p = 0\ \frac{\text{kg}}{\text{ms}^2}$
Initial condition	Velocity	$[u_x, u_y, u_z] = [0, 0, 0]\ \frac{\text{m}}{\text{s}}$
Initial condition	Turbulent kinetic energy	$k = 0.347\ \frac{\text{m}^2}{s^2}$
Initial condition	Turbulent dissipation	$\epsilon = 0.1\ \frac{m^2}{s^3}$

One now describes the boundary conditions. The inlet is set as a velocity inlet. The velocity profile is defined as introduced in chapter 2, equation 2.29, with the von Kármán constant $\kappa = 0.42$ [38] and a roughness length of $y_0 = 0.0002$ m [47]. The friction velocity u_* was calculated for a reference velocity of $v_{\text{ref}} = 10\ \frac{\text{m}}{\text{s}}$ at the reference height of $y_{\text{ref}} = 90$ m (hub height). The turbulent conditions are specified trough the turbulent kinetic energy and the turbulent dissipation, see chapter 2 equations 2.31 and 2.32 [38]. Note that the inlet velocity and turbulent dissipation vary with the altitude, while the turbulent kinetic energy remains constant. The outlet is defined as a pressure outlet with the static pressure $p = 0\ \frac{\text{kg}}{\text{ms}^2}$. The definition of the plate is always crucial in ABL modeling. It was set as a wall with the no-slip condition and a rough surface. For the calculation of the wall function several constants need to be defined. They are $E_C = 9$ and $C = 0.253$ [1].

Moreover, the so-called roughness height r_h is calculated as

$$r_h = \frac{Ey_0}{C} = 0.0071 \text{ m}, \tag{3.1}$$

according to the *Star-CCM+* user guide [1]. The remaining surfaces are set as symmetry planes.

3.3 LES Simulation

The LES was performed on the basis of the precursor RANS simulation and is described in this section. As a turbulence model the Smagorinsky Subgrid-Scale model is chosen. Different models were tested and this one was found stable for this setup. It is an implicit unsteady, 3D simulation of second order, with a time step of $\Delta t = 0.05$ s. This time step fulfills the CFL number on the one hand and is not too large to cause inaccuracy for the aero-elastic analysis with *FAST* on the other. The total simulation time is 2400 s, leading to a total number of 48000 time steps. The number of inner iterations is 5. The flow needs 600 s to pass the domain. After roughly 1.5 flow passes (1000 s or 20000 time steps), the data is expected to be converged and data is recorded for the following 1400 s. Mean values for the results are averaged over the this interval. The fluid characteristics remain similar to the RANS simulation, as well as the reference values.

The boundary conditions are defined as follows. For the velocity inlet a velocity profile from the precursor RANS simulation is applied. Furthermore, the synthetic turbulence is specified with the turbulence intensity and turbulent length scale. The turbulence intensity is defined as $I = 0.047$, while the turbulent length scale equals $l_0 = 229$ m. These values are obtained from the precursor RANS simulation at hub height (90 m). Similar as the RANS simulation, the outlet is defined as a pressure outlet, with a value of $p = 0 \ \frac{\text{kg}}{\text{ms}^2}$. The bottom plate is defined as a wall with the no-slip condition. However, *Star-CCM+* leaves no option for a rough wall in LES. Apart from that the other surfaces are defined as symmetry planes.

For the creation of a transient flow field for the *FAST* simulations a presentation grid was set up to capture the flow around the two turbines. It range from $y = 19.875$ m to $y = 161.125$ m in the wall-normal direction and from $z = 1929.4$ m to $z = 2070.6$ m in the spanwise direction. Its resolution is 60x60 grid points.

3.4 Actuator Disk and Actuator Line Model

For the ADM and ALM the identical setup as for the LES is used. That includes the applied models, initial conditions, fluid characteristics and reference values, as well as the boundary conditions. However, two Actuator Disks are placed in the domain, with their center at $[x, y, z] = [1999.375, 90, 2000]$ m and $[x, y, z] = [3999.375, 90, 2000]$ m. Note that the locations differ slightly from the previously introduced locations. This is because the center of each turbine must not

be between two cells. The differences in terms of the mesh were already presented, now the physical models for the AD and AL model are discussed.

The ADM only requires few information. The performance of the wind turbine is specified as a function of the wind speed. Therefore, the generated power and thrust coefficients are defined within a table for the wind speed according the description from the NREL [23]. The disk geometry is specified with an inner radius of $r_{\text{in}} = 1.5$ m and an outer radius of $r_{\text{out}} = 63$ m, whereas the thickness is $\delta = 4.5$ m [23]. The normal direction is perpendicular to the inlet surface, pointing in streamwise direction. Moreover, the inflow for the disk needs to be specified. It was defined according to the *Star-CCM+* manual [1], setting the inflow plane radius slightly larger than the actual disk (about 10 %), which leads to a radius of $r = 70$ m. The offset of the plane is 12.6 m, which is 10 % of the diameter as well. Finally, the rotation rate is defined as the operating point specified as 12.1 rpm [23].

The ALM requires more details of the rotor blades including airfoil properties. Therefore, the blade is divided into 18 nodes. For each node a table is provided, delivering the lift coefficient C_l and the drag coefficient C_d as a function of the angle of attack (AOA) and Mach number. Moreover, the chord distribution is tabulated as the chord length for each node over the normalized span (i.e. radius divided by the current location). Similarly, the aerodynamic twist is given for the normalized span. Similar to the ADM, all tables can be found in the description of the NREL [23]. As the ALM is originally developed for helicopter applications, a sweep angle can be specified, but for the current study it is a constant value of 0 radian. The same goes for the disk stick and disk flap specification. For the geometry the thickness is defined as 1.25 m, since at least 3 cells should cover the actuator disk [1]. Despite that, the geometry is defined identical to the ADM, as well as the rotation rate. The azimuthal disk resolution is set to 7 and the radial resolution to 49 [1]. No tip-loss correction is applied for the present study.

3.5 Aero-elastic Simulation

Finally, the aero-elastic simulations using *FAST* are discussed. After performing the LES, the transient velocity field obtained from each presentation grid is transmitted to *FAST*. On this basis the aero-elastic analysis is conducted. The total simulation time is 630 s with a time step of 0.005 s. These are standard values for structural dynamic simulations of wind turbine's. The first 30 s are not included in the assessment, because of instationary behaviour of the turbine at the beginning of the simulation. For the general setup the standard file for the *OC3 Tripod* configuration is used [24]. With this setup two simulations are performed, one with the wind field from the CFD simulation and one with the spectral wind field.

4
Results

In this chapter one presents the results of this project. The chapter is divided into three sections. The first section assesses the quality of the Reynolds-Averaged Navier-Stokes (RANS) simulation as well as the Large Eddy Simulation (LES), which build the foundation for further investigations. Therefore, the velocity field as well as turbulent quantities such as the turbulent kinetic energy k, the turbulence intensity I, the Reynolds stresses and the turbulent length scale Λ are discussed and compared to the literature. All these quantities are mean values, computed over the interval explained in chapter 3. Moreover, the instantaneous field of the LES is discussed. For this one conducts a spectral analysis of the instantaneous velocity field.
In the second section one presents the results from the analysis with *FAST*. One compares the dynamic responses of the wind turbines calculated for a spectral wind field with the responses resulting from the CFD-generated velocity field.

Finally, in the third section one discusses the results from the Actuator Disk Model (ADM) and Actuator Line Model (ALM) simulations. The flow quantities such as velocity v_i, turbulent kinetic energy k, Reynolds stresses and the turbulent intensity I are presented. Furthermore, outputs specifically from the virtual disk, i.e. power and thrust are presented and compared with the results from the *FAST* calculations.

4.1 Atmospheric Boundary Layer Modeling

In the following different flow characterstics are presented to study the quality of the conducted RANS and LES simulations. All quantities are shown for the location of wind turbine 2 (if not stated otherwise), since it is expected that the flow is fully developed at this location. Note that in the RANS and LES simulations the turbines are not included. Therefore, the results in this sections are shown in the absence of the turbines.

4.1.1 Time-Averaged Flow Field

First one presents the mean flow characteristics. In figure 4.1 the streamwise velocity component versus the altitude is shown according to the logarithmic law (see chapter 2, equation 2.29), the RANS simulation and the LES. One can see that both CFD

simulations cover the theoretical mean velocity very well. In the near turbine region the percentage error for both profiles is below 1 %.

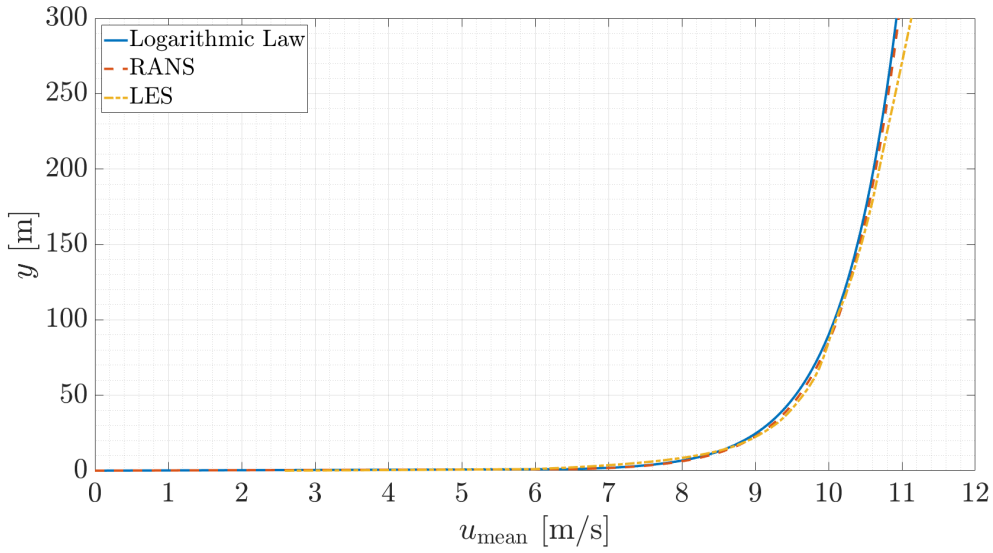

Figure 4.1: Comparison of the mean streamwise velocity component between the logarithmic law according to Richards & Hoxey, the RANS simulation and the LES at the location of turbine 2

The profile of the turbulent kinetic energy (see 2 equation 2.35) is plotted against the altitude in figure 4.2. The left figure shows the distribution for k obtained by the RANS simulation, while the right one shows the results from LES.

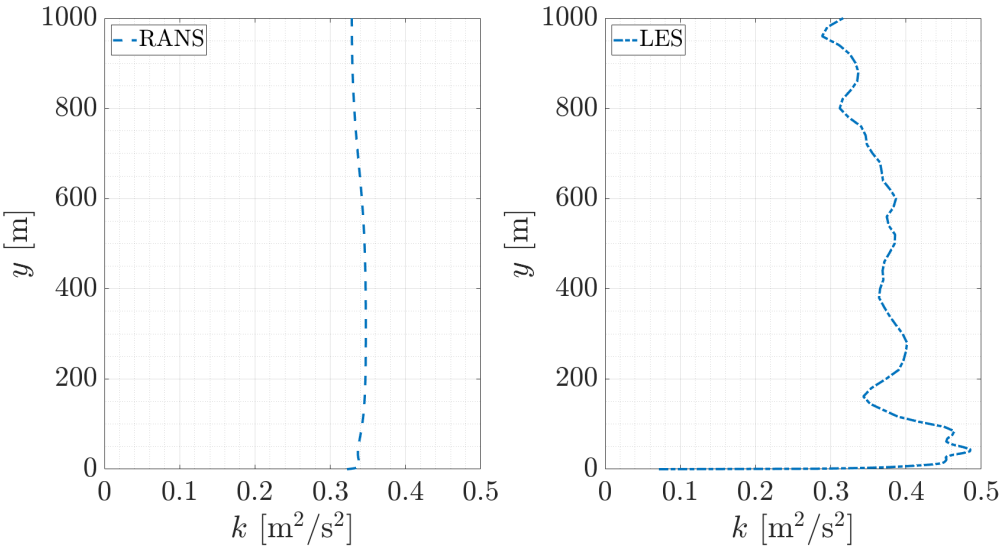

Figure 4.2: Comparison of the turbulent kinetic energy profiles between the RANS simulation and LES at the location of turbine 2

One can see that the RANS simulation gives a rather uniform profile, while the distribution of k calculated by the LES is unequally distributed. Furthermore, the

values for k simulated with LES approach the uniform distribution of the RANS values. Considering the inlet conditions of the RANS simulation, it seems comprehensible that the profile is uniform around the initial value for the inlet, since the inlet conditions were set to create a homogeneous profile [38].
In terms of the LES the values for k near the ground are the highest. This seems reasonable, when looking at the transport equation for k. It is produced either due to large velocity gradients or due to high Reynolds stresses. Since the velocity gradients are the largest in the near wall region, the production of k is also high. This also matches the profiles of the Reynolds stresses, which is discussed down below [11].

Another important turbulence parameter is the turbulence intensity, which was defined in chapter 2 equation 2.37. It is presented in figure 4.3 and plotted against the altitude. One can see a very smooth profile for the RANS simulation, while the profile for the LES is a bit uneven, similar to the profile of k. In both cases the turbulence intensity is decreasing with the height, which is due to higher velocities with higher altitudes. The turbulent fluctuations do influence these profiles, but the influence of the velocity is stronger due to higher magnitudes.

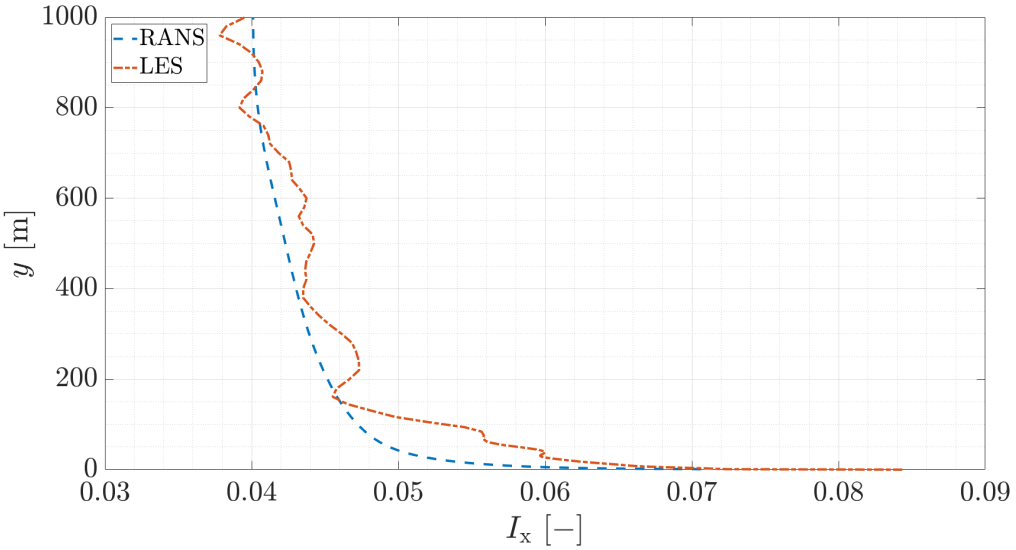

Figure 4.3: Comparison of the turbulence intensity profile between the RANS simulation and LES at the location of turbine 2

Figure 4.4 shows the last graph for the RANS results. The turbulent length scale Λ is plotted versus the altitude. It is defined as

$$\Lambda = \int_0^\infty R(\Delta x)\mathrm{d}x, \tag{4.1}$$

where R is the spatial correlation as a function of the distance Δx between the locations, for which the correlation is calculated. It characterizes the largest eddies at the respective location. One can see the length scale increasing linearly with the height up to 800 m, where it seems to be converging towards a value of 2000 m.

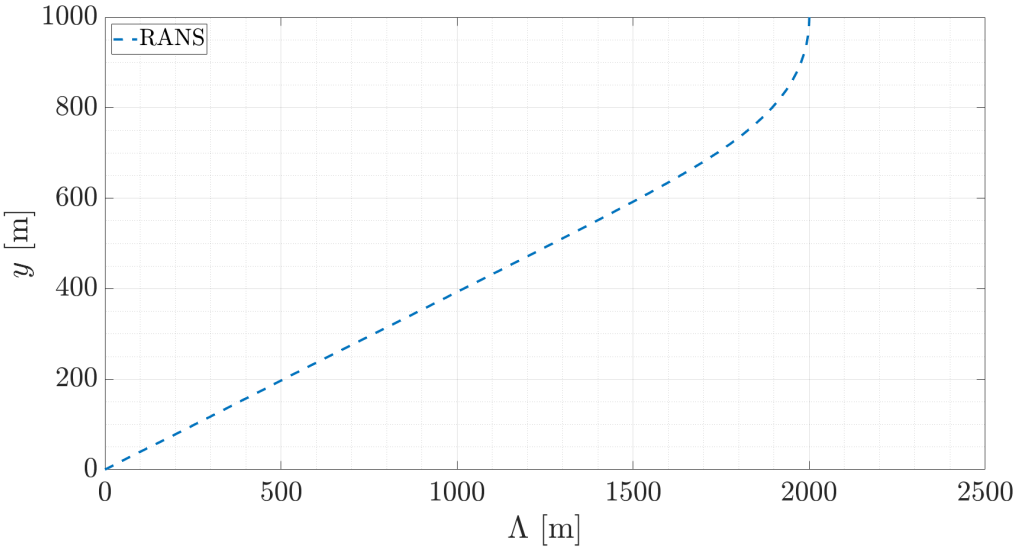

Figure 4.4: Turbulent length scale of the RANS simulation at the location of turbine 2

The turbulent length scale is an important parameter for the turbulence generation within the LES as well as for the meshing. At the inlet of the LES the turbulence must be characterized. In this study it was done by providing the turbulence intensity and the turbulent length scale, see chapter 3. For the turbulent length scale the value from the precursor RANS simulation at hub height was taken ($\Lambda = 229$ m). Nevertheless, regarding a general guideline $\Lambda = \kappa y = 0.42 * 90$ m $= 37.8$ m [3], this value seems to be rather high. Considering the mesh, this value is also important. Since it provides information about the size of the eddies, the mesh used in LES needs to be fine enough to capture the energy containing scales. In the present study the base size is 20 m, leading to 2 cells to capture the largest eddies at hub height in the x and z direction. However, note that the hub height location is within the Prism Layer and therefore refined in y direction. This is an indicator that the turbulence is captured well at least in its larger scales with the chosen mesh in the LES. In terms of the ADM and ALM the regions around the hub height are even more refined, see chapter 3.

Now the Reynolds stresses are presented and compared to a simple channel flow [11]. The normal stresses are plotted in figure 4.5 against the altitude. All stresses are zero near the wall and then start growing with height. As expected from the literature the streamwise component of the normal stresses is the largest, while the wall-normal component is the smallest near the wall. This is because of the mean flow direction and the damping of the turbulent fluctuations of the wall, respectively. After growing near the wall the y and z component reach a near uniform profile. The streamwise component first is characterized by a strong increase followed by a decrease in magnitude and experiences higher fluctuations over the entire domain. According to the literature all stresses should decrease with the height after the initial increase near the wall, but in the present study one cannot see that trend. When comparing the normal stresses to the turbulent kinetic energy, one can see

that k is smaller than the streamwise component of the stresses. This is as well predicted by the literature and also very logical due to the definition of k.

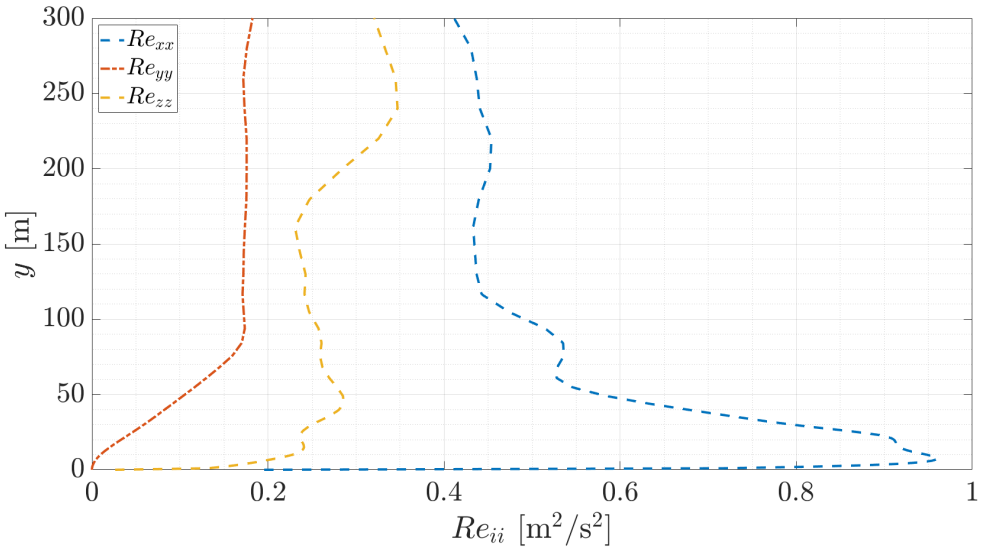

Figure 4.5: Normal stresses of the LES at the location of turbine 2

The shear stresses are plotted against the altitude in figure 4.6. One can see fluctuations for all components, even with a relatively small magnitude. However, this result does not seem to be correct, since Re_{xy} should be negative, while Re_{xz} and Re_{yz} remain zero. Overall, one can say that the general trend for the normal components Re_{xx}, Re_{yy} and Re_{zz} seems to be correct, however, the results are not very accurate. Furthermore, the results for the shear stresses do not agree with the literature. This may be caused by short simulation and sampling time.

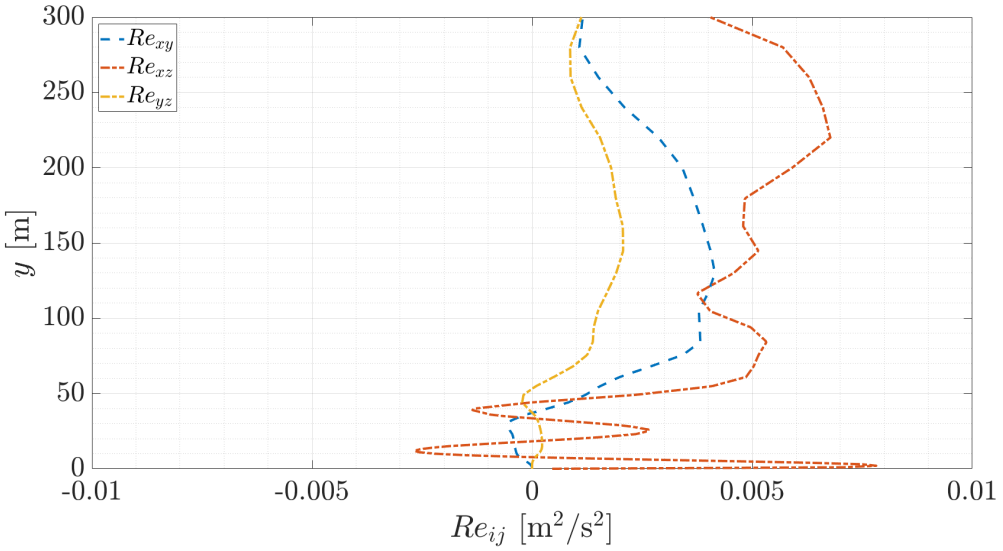

Figure 4.6: Shear stresses of the LES at the location of turbine 2

4.1.2 Instantaneous Flow Field

One now discusses the instantaneous flow field obtained by the transient LES. For this one assesses different locations in the domain. On the one hand a single point at the hub height of the second turbine is investigated, on the other a straight line in the spanwise direction from the presentation grid at hub height. In figure 4.7 the velocity components in all three directions are plotted over the time at hub height at turbine 2. One can see that the non-streamwise velocities v, w are fluctuating around values very close to 0 $\frac{\mathrm{m}}{\mathrm{s}}$, as expected. The streamwise component u is fluctuating around 10 $\frac{\mathrm{m}}{\mathrm{s}}$, which can be expected as well from the mean velocity profile, see figure 4.1.

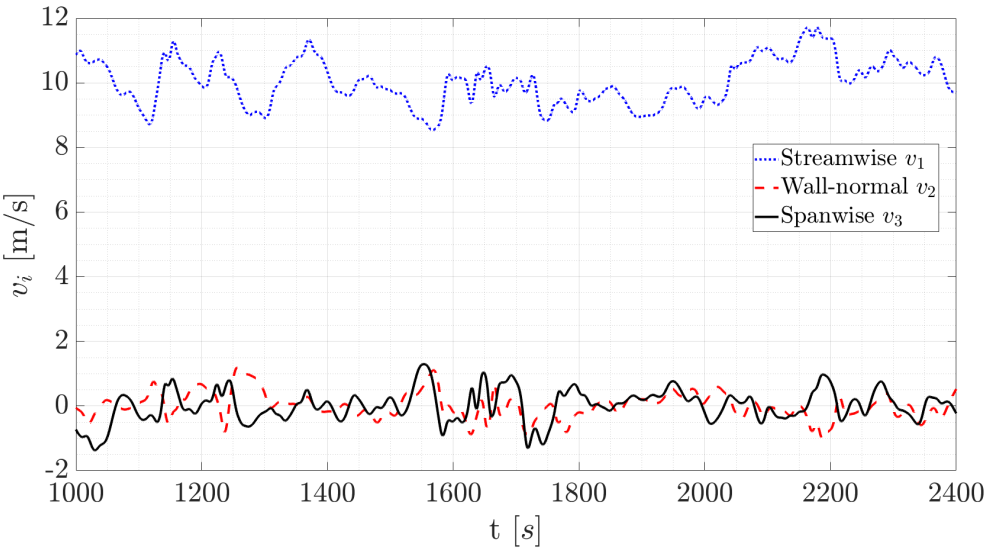

Figure 4.7: Instantaneous velocity components at hub height at turbine 2

When performing a discrete Fourier transformation one obtains the energy density spectrum of the instantaneous velocity in the spanwise direction. This indicates the variety of scales resolved in the LES. It is shown in figure 4.8 as a function of the frequency. On the left side, there are the lower frequencies and one can find the larger scales of the flow field. With higher frequencies the scales become smaller and in LES, at some point these scales are then modelled and not resolved.
Overall, one can see that the LES resolves the larger scales well at hub height. However, when looking at the discontinuity in the mid-range frequencies, one notices that smaller scales are not resolved as predicted by the Kolmogorov law (black line) [11].
This is mainly due to the mesh resolution. If the mesh is not fine enough, it cannot capture smaller scales, but filters them, as discussed in chapter 2, section 2.2.4. Note that this spectrum will differ when looking at different altitudes. Towards the ground, the turbulent scales become smaller and therefore the mesh needed for a good resolution becomes finer.

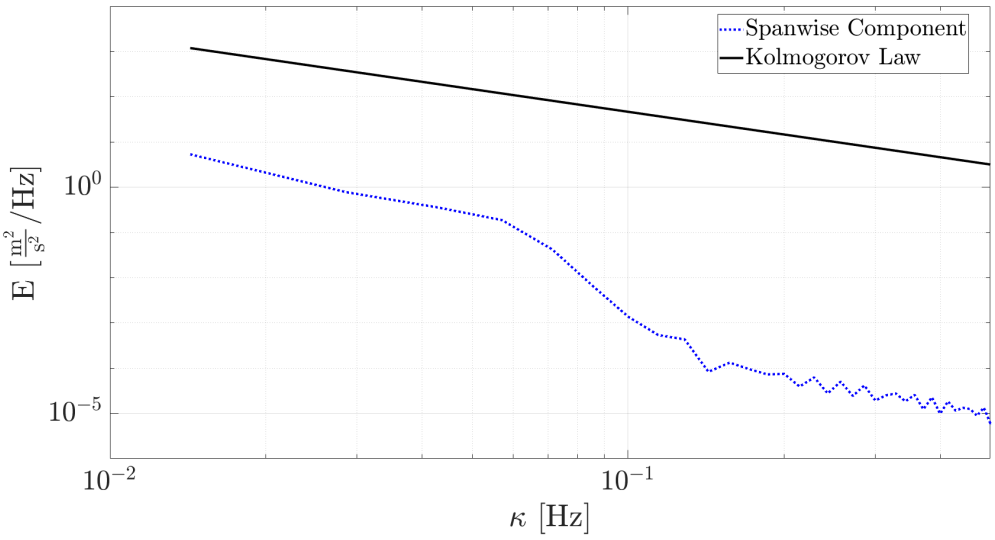

Figure 4.8: Energy density spectrum of the instantaneous spanwise velocity component at hub height at turbine 2

Furthermore, the correlation of the velocity components in space is investigated at hub height as shown in figure 4.9.

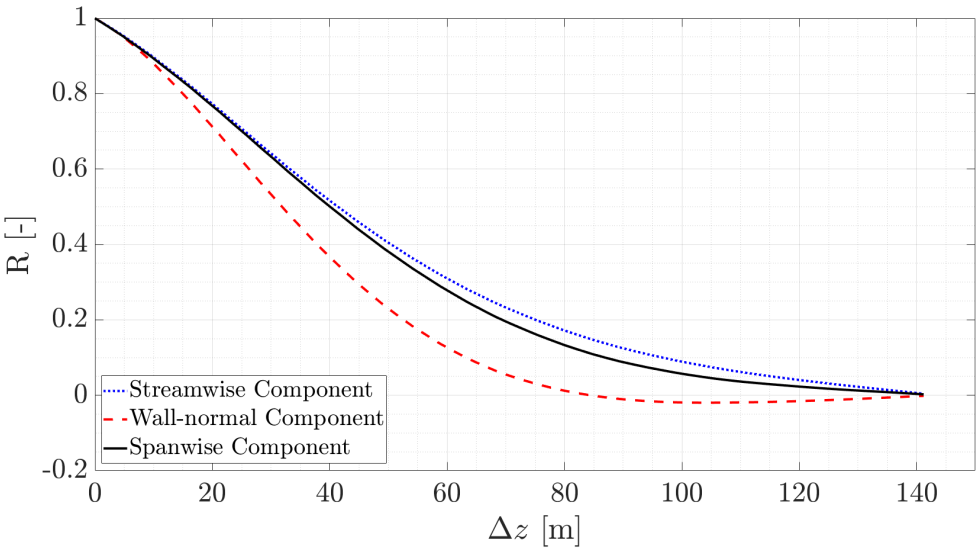

Figure 4.9: Spatial correlation of the velocity components in the z direction at hub height at turbine 2

It is defined as

$$R = \frac{\overline{u'(x,y,z,t)u'(x,y,z+\Delta z,t)}}{\sqrt{u'^2(x,y,z,t)}\sqrt{u'^2(x,y,z+\Delta z,t)}}, \tag{4.2}$$

which is the two-point correlation in space of the velocity fluctuations in z direction (spanwise) normalized with the root mean square value of the velocity fluctuations.

One assumes, that the turbulent structures correlate with each other within the largest eddies (turbulent length scale) at a certain location. One can now calculate the turbulent length scale by integrating over the correlation, see equation 4.1. One should integrate only to the first zero, since after that point there is no physical correlation. The fluctuation in x and z directions almost reach zero at 140 m (which is the length of the presentation grid), while the y component reaches zero around 82 m. This leads to the turbulent length scales shown in table 4.1.

Table 4.1: Turbulent length scale calculated from the spatial two-point correlation of the velocity fluctuations in z direction

x Component	y Component	z Component
47.83 m	34.07 m	44.95 m

These values seem reasonable, since the turbulent length scale can be calculated as a rule of thumb as $\Lambda = 37.8$ m [3], as introduced earlier in this section.

4.2 Wind Turbine Response

In this section one presents the results from the *FAST* simulations, showing the dynamic response of the wind turbines. Therefore, one compares the *FAST* simulation with a spectral velocity field versus the simulation with the flow field calculated by the LES for turbine 2. Several important characteristics are presented here, whereas further outputs are attached to appendix A. Moreover, one can find the mean values and standard deviations of the results presented below in table 4.2 at the end of this section.

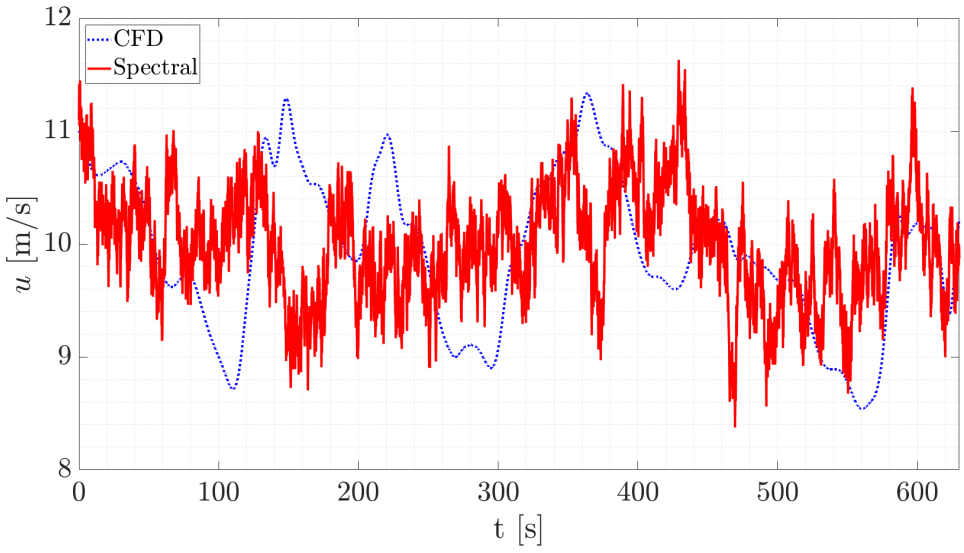

Figure 4.10: Comparison of the instantaneous streamwise velocity extracted from the *FAST* simulation at hub height at turbine 2 of the spectral-based versus the CFD-based flow field

First, the instantaneous streamwise velocity at hub height and turbine 2 is shown in figure 4.10 over the time. The mean streamwise velocity of both simulation is identical with $v_1 = 9.99\ \frac{\mathrm{m}}{\mathrm{s}}$. However, the standard deviation of the CFD-generated velocity field equals $0.67\ \frac{\mathrm{m}}{\mathrm{s}}$ and is a bit higher than the standard deviation of the spectral flow field, which is $0.5\ \frac{\mathrm{m}}{\mathrm{s}}$.

Similar trends can be seen in figure 4.11 as well, showing the rotor speed of turbine 2 over the time.

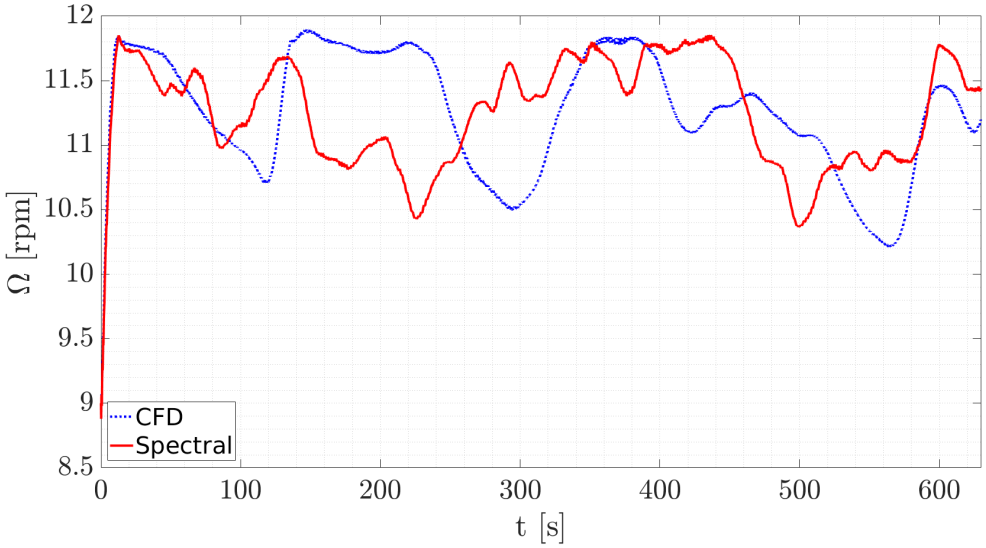

Figure 4.11: Comparison of the rotor speed of turbine 2 of the spectral-based versus the CFD-based *FAST* simulation

The rotor speed of the CFD-based calculation appears to have a nearly periodic character. First the speed decreases, followed by an increase to some sort of plateau. After that there is a small negative peak, followed by a small plateau again. However, one has to conduct a larger number of studies to either validate this statement or disprove it. In contrast to that, one cannot see a clear pattern in the spectral-based simulation. When looking at the statistics one can see that both methods lead to the same mean rotor speed of 11.26 rpm. However, the standard deviation of the spectral method is 0.42 rpm and therefore a bit lower than the CFD method with 0.47 rpm.

The generated power of turbine 2 is plotted over the time in figure 4.12. As expected one can see the shape of the rotor speed (figure 4.11), as it is one of the main factor for the generated power. The mean generated power predicted by the spectral-based simulation equals 3.3 MW and is a bit lower than the predicted power from the CFD-basd simulation, which is 3.38 MW. However, the standard deviation is lower as well with a value of 407.04 comparing to the CFD-based simulation with a value of 506.51.

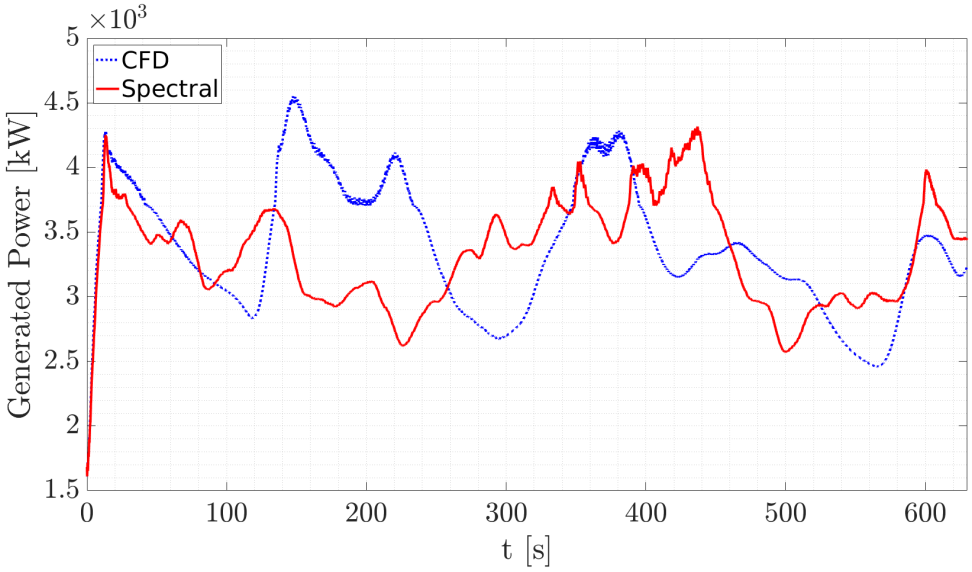

Figure 4.12: Comparison of the generated power of turbine 2 of the spectral-based versus the CFD-based *FAST* simulation

Finally, the blade deflection at the in and out plane of turbine 2 is plotted over the time in figure 4.13. One can see a positive out plane deflection in both cases around 4.6 m for the spectral case and 4.62 m in case of the CFD-generated field. The standard deviation for the spectral method equals 0.41 and is lower than the CFD method, which is 0.47 m. The in plane deflection is slightly negative around −0.46 m and −0.47 m for the spectral velocity field and CFD velocity field, respectively. Again the standard deviation for the spectral method is slightly lower (0.34 m) than the CFD method (0.35 m).

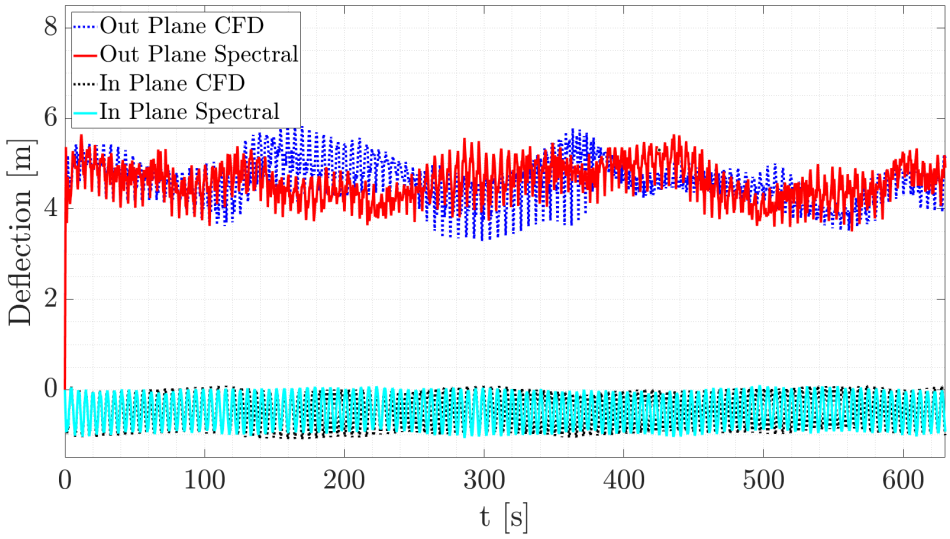

Figure 4.13: Blade deflection of turbine 2 of the spectral-based versus the CFD-based *FAST* simulation

While the out plane deflection shows stronger fluctuations, the inner deflection is nearly fluctuating around a constant value, due to higher stiffness of the blades near the hub region. Furthermore, the algebraic sign from the out and in plane deflection is different, which seems logical when considering the bending curve of the blade.

An overview over the presented results presented so far is shown in table 4.2 for better comparison.

Table 4.2: Output from the FAST simulations with a flow field from spectral analysis as well as from CFD simulations

	Spectral Method		CFD Method	
Quantity	Mean	Std. Deviation	Mean	Std. Deviation
Streamwise Velocity $[\frac{\mathrm{m}}{\mathrm{s}}]$	9.99	0.5	9.99	0.67
Rotor Speed [rpm]	11.26	0.42	11.26	0.47
Inner Deflection [m]	-0.46	0.34	-0.47	0.35
Outer Deflection [m]	4.6	0.41	4.62	0.47
Rotor Torque [kNm]	$2.99 \cdot 10^3$	266.9	$3.03 \cdot 10^3$	339.4
Generated Power [kW]	$3.33 \cdot 10^3$	407.04	$3.38 \cdot 10^3$	506.51

Overall, one can state that both methods generate results very close to one another. However, this can be expected, since a neutral boundary layer with flat terrain (offshore) is investigated in the present study. Moreover one can say that the CFD simulation is capable of producing an appropriate velocity field for the investigated case, while the spectral field was set up in a way, that the outcome is as desired (inverse engineering). Nevertheless, there are multiple benefits of using CFD to generate the flow field. Most importantly the CFD analysis is not limited in the way spectral analysis is. With CFD one can investigate the stability conditions of the ABL as well as the influence of complex terrain, which is not possible through spectral analysis. CFD is therefore capable of reproducing a more realistic environment. However, one has to keep in mind, that the CFD results need to be validated, especially for complex boundary conditions.

4.3 Actuator Disk and Actuator Line Model

In the last section of this chapter the results from the Actuator Disk and Actuator Line model simulations are discussed. One presents the overall flow characteristics first and afterwards discusses the thrust and torque calculation of these two and compare it to the *FAST* simulations.

To get a general idea of the flow field around the Actuator Disk, one presents the streamwise velocity component at different locations before and after turbine 1 in figure 4.14. One can see the velocity plotted against the altitude for the ADM and ALM, respectively. On the left the streamwise velocity is shown for 4 D upstream of the Disk. This is the mean streamwise velocity profile, that was already introduced

within the RANS and LES results, see figure 4.1. Next to it the velocity profiles are shown for 0.1 D upstream of the Disk, which is 12.6 m. It is noticeable that the ADM reduces the velocity significantly less than the ALM. Furthermore, the profile is rather uniform, while the ALM describes a stronger decrease of the velocity alongside the blades. The decrease at hub height is not that strong compared to the blades.
The figure next to it shows the velocity directly at the disk location of turbine 1. Again, the two profiles show great differences. Similar to the previous figure, the velocity is reduced more in case of the ALM in the blade area, while it is nearly maintained at hub height. Furthermore, one can clearly see the disk geometry in case of the ADM. The velocity decay here is very sharp in the outer disk region, while it is smoother when resolved with the ALM.

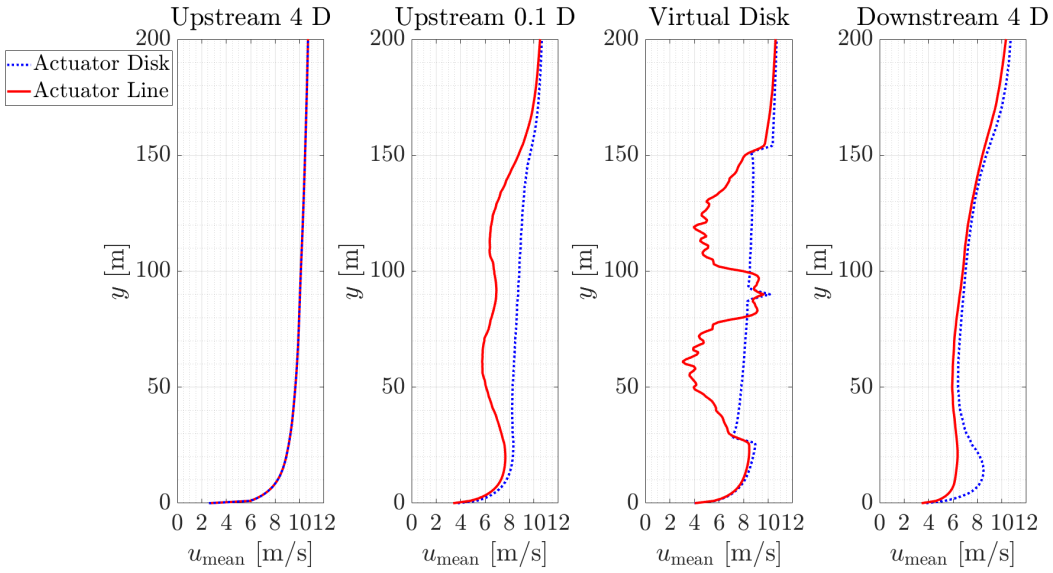

Figure 4.14: Comparison of the streamwise velocity component between the Actuator Disk and Actuator Line simulation near turbine 1

Finally, on the right side the velocity profile at the location 4 D downstream of the disk is presented. Both profiles are relatively uniform. However, one still notices a decrease of the streamwise velocity. This knowledge is especially important when putting more turbines in the downstream direction. However, since the distance between the two turbines in the present study measures 2000 m or about 15.8 D, one cannot see a clear difference between the velocity profiles of the two turbines, see appendix A.8.

Another important flow characteristic is the turbulent kinetic energy. It is shown in figure 4.15 versus the altitude. The locations are 0.1 D upstream of the Virtual Disk, at the disk and 4 D downstream of disk 2. Most importantly, one can see a significant increase of the turbulent kinetic energy in all three figures. Even 0.1 D upstream of the turbine (left figure), the turbulent kinetic energy in case of the ADM equals $k = 0.76\ \frac{m^2}{s^2}$, while it is $k = 0.9\ \frac{m^2}{s^2}$ for the ALM at hub height. This is more than double the value of the initial flow field without the Actuator Disks.

However, while the profiles upstream of the disk are rather uniform, one can see the characteristic shapes of each method when looking directly at the turbine location, shown in the middle. Unlike the streamwise velocity, the shape of the disk in case of the ADM cannot be seen that sharp. The same trend is noticeable for the ALM. Further away from the turbine, in the right figure, the profiles are more uniform, although one can still clearly see the effect of both models. In case of the ALM the profile reaches values of about ten times the initial value and equals $k = 3.77\ \frac{\mathrm{m}^2}{\mathrm{s}^2}$, while in case of the ADM the turbulent kinetic energy is only about four times the initial value at hub height, which is $k = 1.22\ \frac{\mathrm{m}^2}{\mathrm{s}^2}$. These profiles indicate higher fluctuation downstream of the disk, induced by each model. This can also be seen when looking at the Reynolds stresses down below.

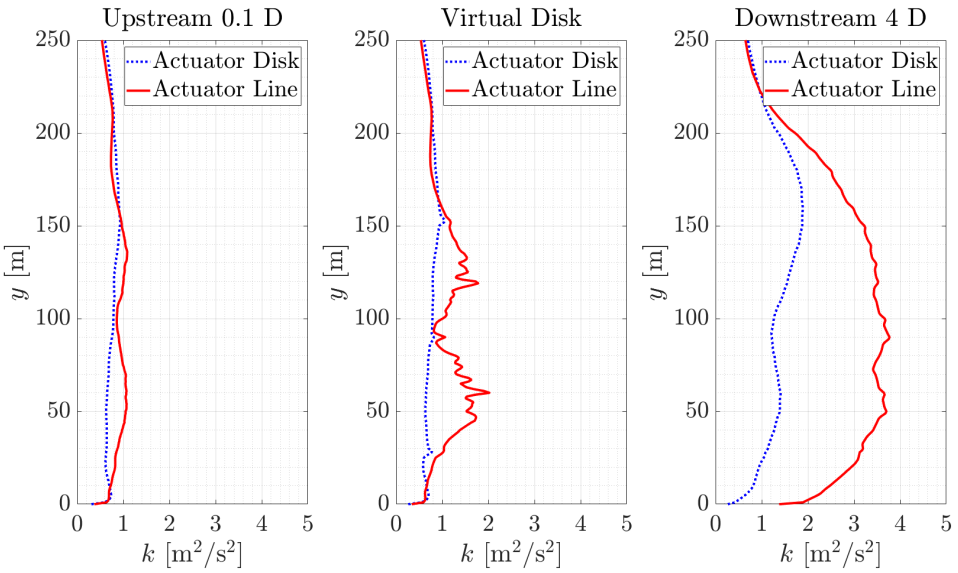

Figure 4.15: Comparison of the turbulent kinetic energy between the Actuator Disk and Actuator Line simulation near turbine 2

The turbulent kinetic energy profiles for the first turbine are shown in the appendix A.9. While the values for the ADM are slightly less at all three positions, the ALM behaves differently. Upstream and at the turbine location, the values for k are less for turbine 1 than for turbine 2 as well. However, at the location 4 D downstream of each turbine, the peak for the first turbine is much higher. Since the models applied to each turbine are exactly the same, one cannot find a logical explanation for this effect. Further studies have to clarify, if it is because of short sampling or it occurs further on.

Further on, the turbulence intensity is shown in figure 4.16 for the investigated locations. One can see that the turbulence intensity in case of the ADM gives a uniform distribution trough out the domain around the value of $I = 0.1$. The ALM behaves very differently, as one can see a strong increase at the location of the blades, while the value at near the hub height nearly equals the ADM. However, for both methods the profiles nearly remains the same in the streamwise direction, respectively. This may seem unexpected, but can be explained with the definition

of the turbulence intensity. As one can see in chapter 2 equation 2.37 it is defined as the fluctuation divided by the mean velocity. In this case these two quantities balance each other which lead to maintain the profile in the streamwise direction. When looking at the turbulence intensity of turbine 1 (appendix A.10), one can see that the ADM produces the same profile for this turbine, while the magnitudes for the ALM are lower than turbine 2. This matches the profile of the turbulent kinetic energy at the location 4 D downstream of turbine 1, as this increases the fluctuations in the flow field. Note that this is only valid for the ALM.

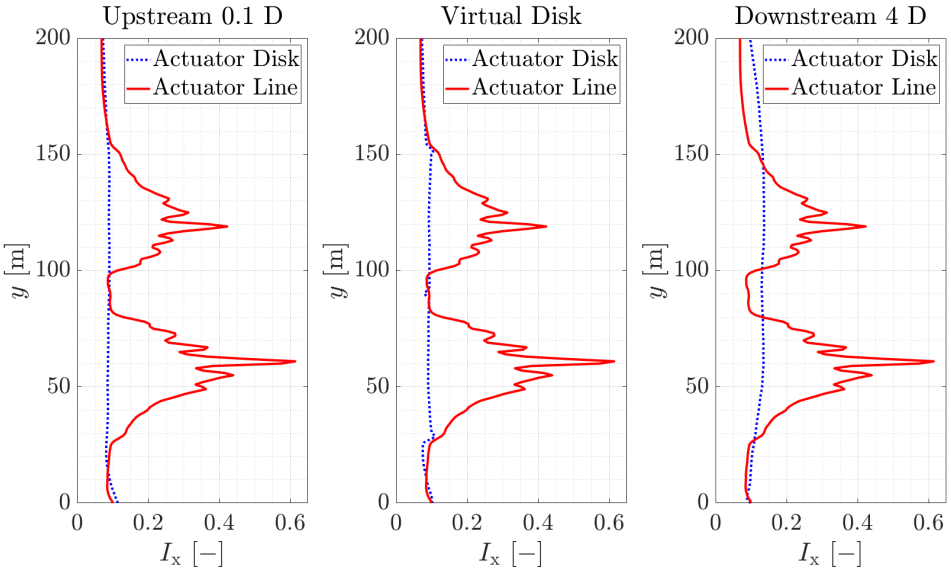

Figure 4.16: Comparison of the turbulence intensity between the Actuator Disk and Actuator Line simulation near turbine 2

One may now assess the Reynolds stresses. First, one discusses the normal components of the Reynolds stresses, i.e. Re_{xx}, Re_{yy} and Re_{zz} in the streamwise, wall-normal and spanwise direction, respectively. The normal component of the velocity field in the streamwise direction Re_{xx} is shown in figure 4.17 versus the altitude. Overall, these fit the characteristics seen from other turbulent quantities so far. The ALM produces high Reynolds stresses in the blade area, while the profile of the ADM is rather uniform before and at the turbine, while showing two characteristic peaks at the 4 D downstream location. This has been seen already in the profiles of the turbulent kinetic energy. Comparing both turbines (see appendix A.11), one can see an increase of Re_{xx} in case of the ADM for all profiles from the first to the second turbine. In case of the ALM one cannot see this trend.

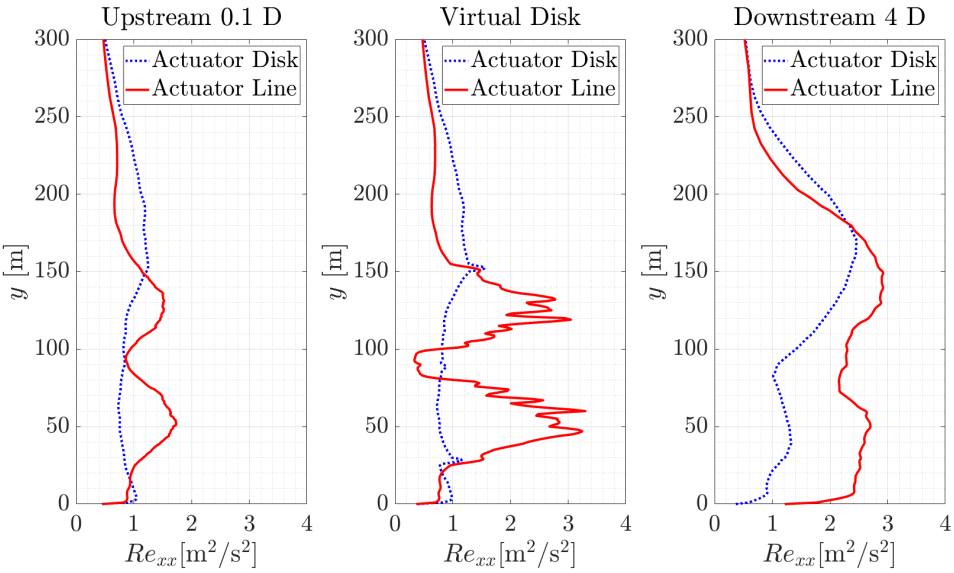

Figure 4.17: Comparison of the normal component Re_{xx} of the Reynolds stresses between the Actuator Disk and Actuator Line simulation near turbine 2

Furthermore, the shear components of the Reynolds stresses Re_{xy}, Re_{xz} and Re_{yz} are simulated in the present study. The shear stress component Re_{xy} is shown in figure 4.18 as a function of the altitude.

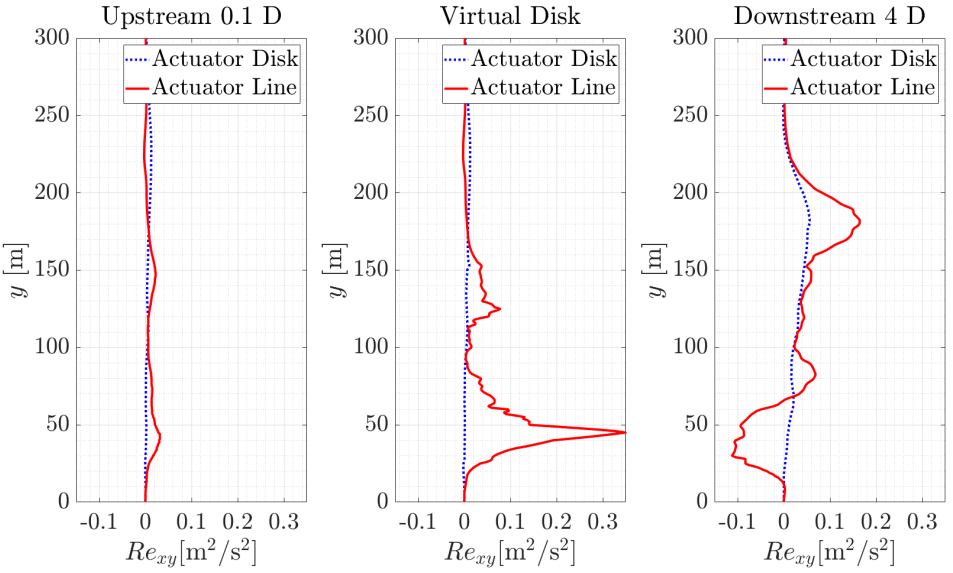

Figure 4.18: Comparison of the shear component Re_{xy} of the Reynolds stresses between the Actuator Disk and Actuator Line simulation near turbine 2

First the shear stresses are very near zero for both models. In case of the ADM this stays the same in downstream direction, although they experience a slight increase in the far wake region. However, the calculation of the ALM shows a different behaviour. There is a very high peak at the turbine location, especially in the region around $y = 50$ m. This might be because of a too short sampling time. One indicator for this could be the shear stress Re_{xy} at 4 D downstream of the turbine. There

the trend is completely reversed. Additionally there is a peak at $y = 180$ m, which is just above the top blade ending. This can be explained by the very high shear that occurs when the momentum from the blade is transmitted to the fluid in the free stream. On the bottom end of the turbine the situation is different because of the ground influence. One explanation could be, that the ground pushes the air in positive y direction, and even increases the shear forces. Furthermore, the air from outside the far wake field is entrained into the wake. This is applying additional shear forces onto the various regions. For the sake of completeness, the remaining stresses are placed in the appendix, see figure A.12 - A.15.

Finally, one discusses the outputs specifically generated by the ADM and ALM, i.e. thrust and torque. In figure 4.19 the thrust is shown over the time calculated by each model. Comparing the mean values and standard deviations, table 4.3, one can see that the ALM predicts a higher thrust force (626 kN) than the ADM (358 kN). Moreover, the standard deviation of the ALM equals 8.47 kN and is therefore less than the standard deviation of the ADM, which equals 33.2 kN. Furthermore, the time to reach a near steady state is shorter and seems to be more stable for the ALM.

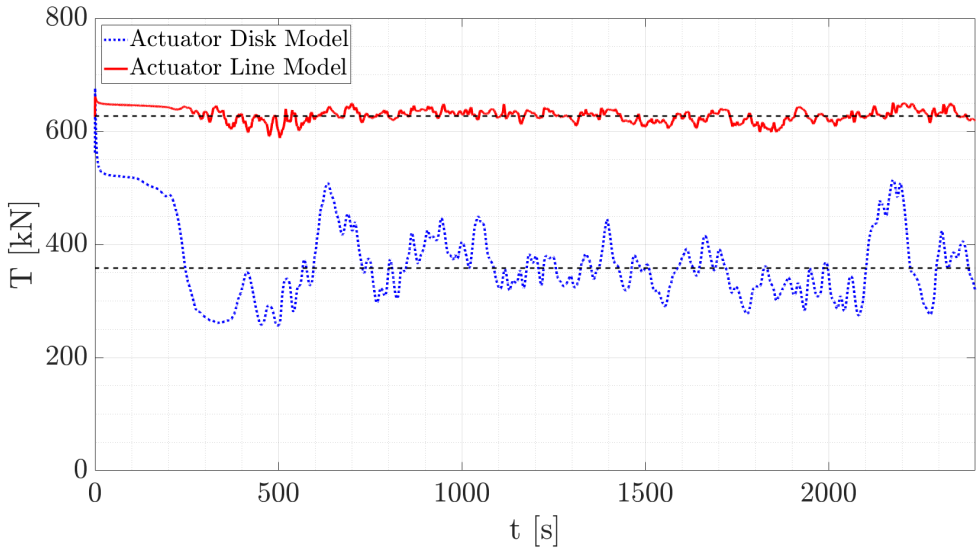

Figure 4.19: Comparison of the thrust between the Actuator Disk and Actuator Line simulation at turbine 2

When looking at the torque distribution in figure 4.20, there is a significant difference between the two calculations. While the ALM predicts a torque at least of the same order as *FAST* (1.88 $\cdot 10^3$ kNm), the ADM predicts the momentum to be a lot smaller (1.32 kNm). A comparison between the standard deviations seems to be inappropriate, since the mean values are of a different order. These results might be explained with the different theoretical background, which the models are based on. However, literature shows, that it is possible to generate accurate results with both models [44]. This should be a topic of further investigations. Nevertheless, when looking at the curve shape, it looks very similar for both models.

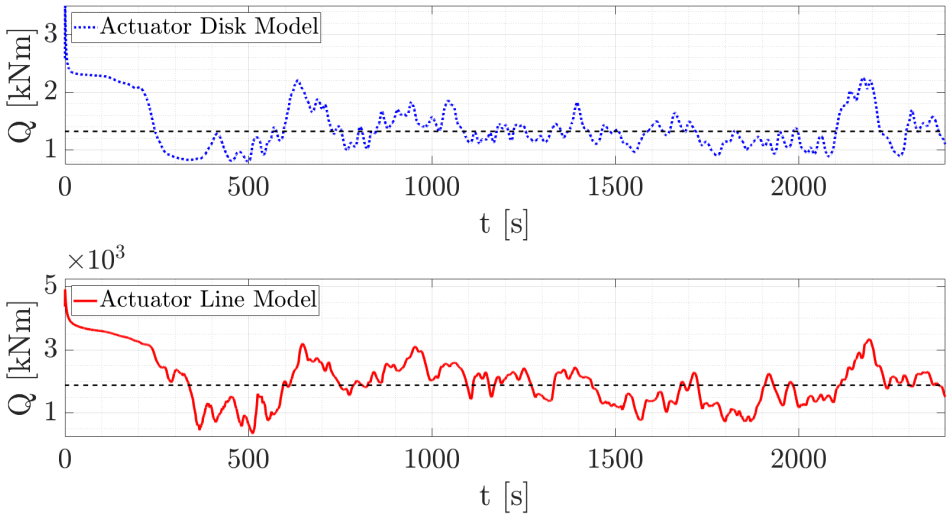

Figure 4.20: Comparison of the torque between the Actuator Disk and Actuator Line simulation at turbine 2

One now presents the mean outputs and standard deviations (denoted by *Std. Dev.*) from the Actuator Disk-, Actuator Line- and *FAST* simulation for turbine 2, see table 4.3. In terms of the *FAST* simulation the CFD-based flow field is chosen for better comparison. The generated power is listed as well. Note that the Actuator Disk and Actuator Line model assume a constant rotation rate, which is specified as 12.1 rpm [23].

Table 4.3: Output from the Actuator Disk Model, Actuator Line Model and FAST simulations for turbine 2

	ADM		ALM		*FAST*	
Quantity	Mean	Std. Dev.	Mean	Std. Dev.	Mean	Std. Dev.
Thrust [kN]	358	33.2	626	8.47	676	58.06
Torque [kNm]	1.32	0.19	$1.88 \cdot 10^3$	456.63	$3.03 \cdot 10^3$	339.4
Power [kW]	1.68	0.23	$2.39 \cdot 10^3$	578.6	$3.38 \cdot 10^3$	506.61

Overall, one can see that both CFD models do not predict the forces and moments like *FAST*. Despite that the performance of the Actuator Disk calculation needs to be further investigated, since it differs significantly from the *FAST* calculations. The Actuator Line method does deviate significantly from the *FAST* solution as well, but at least predicts forces and moments of the same order. Reasons for that might the rotation rate and control systems applied to the turbine. Within the ADM and ALM the rotation rate is constant during the entire simulation, whereas it is adapted continuously within *FAST*. Moreover, *FAST* includes a control system, which is not included in the ADM or ALM. Implementing the effect of the tower and nacelle on into the ADM and ALM in *Star-CCM+* might be an important aspect as well. Nevertheless, the thrust predicted by the Actuator Line model is relatively close to the one predicted by *FAST*.

5

Conclusion

One now draws the conclusions for the present study. First of all, the wind field in the Atmospheric Boundary Layer (ABL) was generated with a Large Eddy Simulation (LES) for an offshore environment. Therefore, a Reynolds-Averaged Navier-Stokes (RANS) simulation was conducted to create the inlet conditions and turbulence specification for the LES. It was found, that both simulations captured the mean velocity field very well, compared to the logarithmic law after Richards and Hoxey [38], see figure 4.1. Moreover, the turbulent kinetic energy is also well described by both methods (figure 4.2). The inlet conditions for the RANS simulation were set to create a homogeneous profile throughout the domain. The turbulent kinetic energy and mean velocity validate the quality of this setup. In case of the LES one can see fluctuations, which may be caused by short simulation and sampling time. Furthermore, the turbulence intensity was investigated, see figure 4.3. A very uniform profile was obtained with the RANS simulation, giving realistic values for the investigated environment. Again, the LES shows a more unequally distributed profile. Moreover, the turbulent length scale was calculated by the RANS simulation (figure 4.4). These values seem to be rather high compared to the literature [3]. In addition to that the Reynolds stresses are not described very accurately by the LES. The normal components of the Reynolds stresses show the general trend compared to the literature, but the accuracy is rather poor, see figure 4.5. A reason for that might be the sampling time, which should be longer for flat terrain. However, the shear components of the Reynolds stresses (figure 4.6) do not seem to be resolved well, as there are several disagreements with the literature [11].
Further investigation was done by looking at the instantaneous flow field of the LES. The instantaneous velocity was decomposed with a discrete Fourier transformation and an energy density spectrum was obtained (figure 4.8). The overall resolution of scales by the LES was found to be good in the larger scales. However, comparing the spectrum to the Kolmogorov law, one can see that the mesh resolution is not fine enough for smaller scales. For the purpose of this study the resolution is still acceptable, since the input for the *FAST* investigations, the velocity field, was of good quality. Lastly a two-point spatial correlation of the instantaneous velocity was investigated for a line of the presentation grid at hub height, see figure 4.9. The turbulent length scale was calculated for that line. It was found that the turbulent length scales obtained are in good agreement with the literature [3].

One of the main objectives of the thesis was to validate the integration of the aero-elastic analysis into the Computational Fluid Dynamics (CFD) process. This was done by transmitting two different flow fields to the aero-elastic solver *FAST*. One

is a spectral flow field, which is provided by *TurbSim* [22], another one is the flow field generated with the LES. Different quantities were investigated over the time, the most important ones are the streamwise velocity, the rotor speed, the generated power and the blade deflection, see figures 4.10 - 4.13, respectively. Overall, a good agreement between these two methods was found by comparing the mean values and standard deviation of these quantities, see table 4.2.

Finally, two methods are tested within the CFD software *Star-CCM+* to model the effect of a wind turbine, without actually resolving its geometry. Therefore, the Actuator Disk Model (ADM) and Actuator Line Model (ALM) were tested and compared to the results obtained with the *FAST* simulation. The overall flow characteristics of these two models are very different. In terms of the streamwise velocity, the turbulent kinetic energy and the turbulence intensity the ADM influences the flow field significantly less than the ALM, see figures 4.14 - 4.16. In terms of the Reynolds stresses no general differences can be described between these models, see figures 4.17 and 4.18 and appendix A.11 - A.15.
Comparing the forces and moments between the ADM, ALM and *FAST* a couple of conclusions can be drawn. In terms of the thrust, the ADM differs from the other two models, while the ALM predicts the thrust relatively close to *FAST*. The standard deviation of the ALM is even less than predicted by *FAST*. In case of the torque, the ALM predicts a torque in the same order of the *FAST* prediction. However, there is still a big difference between the two methods. The prediction of the ADM is in a different order than the other two simulations.

These results lead to suggestions for future work and improvements. Based on the literature and this study, several aspects can lead to better performance of the ADM and ALM [31][44]. One of them is the implementation of the tower and nacelle influence on the simulation. In the aero-elastic solver *FAST* this feature is already available, but in *Star-CCM+* it still remains a topic of future work. Furthermore, the influence of the mesh should be investigated, since according to the literature it influences the power output of the ADM and ALM. Moreover, when setting up the Actuator Disk in *Star-CCM+*, an inflow plane is determined, which is then taken for the calculation of the forces. The size and distance to the Actuator Disk might also be influence on the calculations and should be further investigated. Lastly, the thickness of the Actuator Disk was defined differently for the ADM and ALM. An optimal thickness for the disk could be also a topic for further investigation.
In terms of the modeling of the ABL the results from the LES were acceptable. However, the calculation of the Reynolds stresses was not satisfying. For this two major points can be investigated. First, as already introduced, the mesh can be refined and the influence on the resolution of the scales can be investigated. Second, the turbulent length scale at the inlet may be changed according to the literature [3] and the effects may be studied. Finally, the simulation and sampling time may be increased.

Bibliography

[1] (2017). *Star-CCM+ Documentation*. Siemens PLM Software.

[2] ABSEnergyResearch (2010). The wind power report - market research report. `http://www.absenergyresearch.com/energy-market-research-reports/renewable-energy-market-research-reports/wind-power/reports/wind-power-report-2010`. Accessed: 2019-02.

[3] Apsley, D. D. and Castro, I. P. (1997). A limited-length-scale k-ε model for the neutral and stably-stratified atmospheric boundary layer. *Boundary-layer meteorology*, 83(1):75–98.

[4] Bechmann, A. (2007). *Large-eddy simulation of atmospheric flow over complex terrain*. PhD thesis, Risø National Laboratory. Risø-PhD-28(EN).

[5] Breton, S.-P. and Moe, G. (2009). Status, plans and technologies for offshore wind turbines in europe and north america. *Renewable Energy*, 34(3):646–654.

[6] Burger, B. (2018). Stromerzeugung in deutschland 2017: Solar- und windenergie übertreffen erstmals kohle und kernenergie. `https://www.ise.fraunhofer.de/de/presse-und-medien/news/2018/stromerzeugung-in-deutschland-2017-solar-und-windenergie-uebertreffen-erstmals-kohle-und-kernenergie.html`. Accessed: 2019-05-31.

[7] Cabezon, D., Hansen, K. S., and Barthelmie, R. (2010). Analysis and validation of cfd wind farm models in complex terrain wakes induced by topography and wind turbines. *Proc. EWEC*.

[8] Chen, J., Wang, Q., et al. (2017). *Wind Turbine Airfoils and Blades: Optimization Design Theory*, volume 3. Walter de Gruyter GmbH & Co KG.

[9] Churchfield, M. J., Lee, S., Schmitz, S., and Wang, Z. (2015). Modeling wind turbine tower and nacelle effects within an actuator line model. In *33rd Wind Energy Symposium*, page 0214.

[10] Davidson, L. (2018). An introduction to turbulence models. `http://www.tfd.chalmers.se/~lada/#allpaper.html`. Accessed: 2019-05-31.

[11] Davidson, L. (2019). Fluid mechanics, turbulent flow and turbulence modeling. `http://www.tfd.chalmers.se/~lada/postscript_files/solids-and-fluids_turbulent-flow_turbulence-modelling.pdf`. Accessed: 2019-05-31.

[12] Deutch, J., Moniz, E., Ansolabehere, S., Driscoll, M., Gray, P., Holdren, J., Joskow, P., Lester, R., and Todreas, N. (2003). The future of nuclear power. *an MIT Interdisciplinary Study, http://web. mit. edu/nuclearpower*.

[13] Emeis, S. (2012). *Wind Energy Meteorology: Atmospheric Physics for Wind Power Generation*. Green Energy and Technology. Springer Berlin Heidelberg.

[14] Energy, G. (2018). Wind turbines continue to grow in size. `https://www.power-technology.com/comment/wind-turbines-continue-grow-size/`. Accessed: 2019-05-31.

[15] e.V., B. W. (2018). Zahlen und fakten, statistische kennziffern zur erfolgsgeschichte windenergie. `https://www.wind-energie.de/themen/zahlen-und-fakten/`. Accessed: 2019-05-31.

[16] Evans, A., Strezov, V., and Evans, T. J. (2009). Assessment of sustainability indicators for renewable energy technologies. *Renewable and sustainable energy reviews*, 13(5):1082–1088.

[17] Hargreaves, D. and Wright, N. (2006). The use of commercial cfd software to model the atmospheric boundary layer. *Cwe*, 2006:797–800.

[18] Hepbasli, A. and Ozgener, O. (2004). A review on the development of wind energy in turkey. *Renewable and Sustainable Energy Reviews*, 8(3):257–276.

[19] Herbert, G. J., Iniyan, S., Sreevalsan, E., and Rajapandian, S. (2007). A review of wind energy technologies. *Renewable and sustainable energy Reviews*, 11(6):1117–1145.

[20] Hucho, W.-H. (2002). *Aerodynamik der stumpfen Körper*. Springer.

[21] Ingram, G. (2011). Wind turbine blade analysis using the blade element momentum method. *Durham University, Durham*.

[22] Jonkman, B. J. and Buhl Jr, M. L. (2006). Turbsim user's guide. Technical report, National Renewable Energy Lab.(NREL), Golden, CO (United States).

[23] Jonkman, J., Butterfield, S., Musial, W., and Scott, G. (2009). Definition of a 5-mw reference wind turbine for offshore system development. Technical report, National Renewable Energy Lab.(NREL), Golden, CO (United States).

[24] Jonkman, J. and Musial, W. (2010). Offshore code comparison collaboration (oc3) for iea wind task 23 offshore wind technology and deployment. Technical report, National Renewable Energy Lab.(NREL), Golden, CO (United States).

[25] Jonkman, J. M., Buhl Jr, M. L., et al. (2005). Fast user's guide. *National Renewable Energy Laboratory, Golden, CO, Technical Report No. NREL/EL-500-38230*.

[26] Kajishima, T. and Taira, K. (2016). *Computational Fluid Dynamics: Incompressible Turbulent Flows*. Springer International Publishing.

[27] Koblitz, T., Sørensen, N., Bechmann, A., and Sogachev, A. (2013). *CFD Modeling of Non-Neutral Atmospheric Boundary Layer Conditions*. PhD thesis, Technical University of Denmark, Denmark.

[28] Kolmogorov, A. N. (1941). Dissipation of energy under locally isotropic turbulence. *Doklady Akademiia Nauk SSSR*.

[29] Kolmogorov, A. N. (1991). The local structure of turbulence in incompressible viscous fluid for very large reynolds' numbers. *Proceedings: Mathematical and Physical Sciences, Turbulence and Stochastic Process: Kolmogorov's Ideas 50 Years On*, 434(1890).

[30] Krohn, S., Morthorst, P.-E., and Awerbuch, S. (2009). The economics of wind energy. *European Wind Energy Association*.

[31] Martinez, L., Leonardi, S., Churchfield, M., and Moriarty, P. (2012). A comparison of actuator disk and actuator line wind turbine models and best practices for their use. In *50th AIAA Aerospace Sciences Meeting including the New Horizons Forum and Aerospace Exposition*, page 900.

[32] Menter, F. R. (1994). Two-equation eddy-viscosity turbulence models for engineering applications. *AIAA journal*, 32(8):1598–1605.

[33] Mikkelsen, R. (2004). *Actuator Disc Methods Applied to Wind Turbines*. PhD thesis, Technical University of Denmark (DTU).

[34] Mortensen, N. G., Landberg, L., Rathmann, O., Frank, H., Troen, I., and Petersen, E. (2001). Wind atlas analysis and application program (wasp). In *Wind Energy Department: Scientific and technical progress 1999-2000*. Wind Energy Department: Scientific and technical progress 1999-2000.

[35] on Climate Change, I. P. (2015). *Climate change 2014: Mitigation of climate change*, volume 3. Cambridge University Press.

[36] Parente, A. and Benocci, C. (2010). On the rans simulation of neutral abl flows. In *Proceedings of the Fifth International Symposium on Computational Wind Engineering (CWE2010) Chapel Hill, North Carolina, USA, May*, pages 23–27.

[37] Porté-Agel, F., Meneveau, C., and Parlange, M. B. (2000). A scale-dependent dynamic model for large-eddy simulation: application to a neutral atmospheric boundary layer. *Journal of Fluid Mechanics*, 415:261–284.

[38] Richards, P. and Hoxey, R. (1993). Appropriate boundary conditions for computational wind engineering models using the k-ϵ turbulence model. *Journal of wind engineering and industrial aerodynamics*, 46:145–153.

[39] Sadrehaghighi, I. (2019). Turbulence modeling - a review. `https://www.researchgate.net/publication/318562275_Turbulence_Modeling_-_A_Review`. Accessed: 2019-05-31.

[40] Sarlak, H., Meneveau, C., and Sørensen, J. N. (2015). Role of subgrid-scale modeling in large eddy simulation of wind turbine wake interactions. *Renewable Energy*, 77:386–399.

[41] Schaffarczyk, A. P. (2014). *Introduction to wind turbine aerodynamics*. Springer.

[42] Schwarze, R. (2012). *CFD-Modellierung: Grundlagen und Anwendungen bei Strömungsprozessen*. Springer Berlin Heidelberg.

[43] Spalart, P. and Allmaras, S. (1992). A one-equation turbulence model for aerodynamic flows. In *30th aerospace sciences meeting and exhibit*, page 439.

[44] Stevens, R. J., Martínez-Tossas, L. A., and Meneveau, C. (2018). Comparison of wind farm large eddy simulations using actuator disk and actuator line models with wind tunnel experiments. *Renewable energy*, 116:470–478.

[45] Stull, R. (1988). *An Introduction to Boundary Layer Meteorology*. Atmospheric and Oceanographic Sciences Library. Springer Netherlands.

[46] Sweden.se (2018). Energy use in sweden. `https://sweden.se/society/energy-use-in-sweden/`. Accessed: 2019-05-301.

[47] Troen, I. and Petersen, E. L. (1989). European wind atlas. *Roskilde: Risø National Laboratory*.

[48] Vasaturo, R., Kalkman, I., Blocken, B., and van Wesemael, P. (2018). Large eddy simulation of the neutral atmospheric boundary layer: performance evaluation of three inflow methods for terrains with different roughness. *Journal of Wind Engineering and Industrial Aerodynamics*, 173:241–261.

[49] Versteeg, H. and Malalasekera, W. (2007). *An Introduction to Computational Fluid Dynamics: The Finite Volume Method*. Pearson Education Limited.

[50] Wallace, J. and Hobbs, P. (2006). *Atmospheric Science: An Introductory Survey*. International Geophysics Series. Elsevier Academic Press.

[51] Walshe, J. D. (2003). *CFD modelling of wind flow over complex and rough terrain*. PhD thesis, © John Walshe.

[52] Wärmeatlas, V. (2013). Verein deutscher ingenieure–11. erweiterte auflage.

[53] Wu, Y.-T. and Porté-Agel, F. (2011). Large-eddy simulation of wind-turbine wakes: evaluation of turbine parametrisations. *Boundary-layer meteorology*, 138(3):345–366.

A

Appendix 1

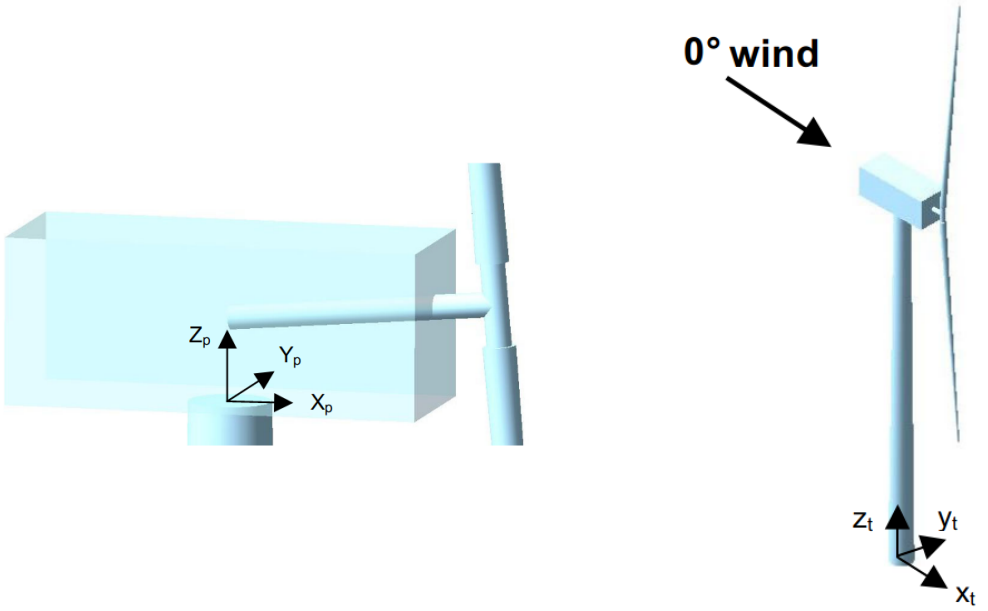

Figure A.1: Tower-top and tower-base coordinate systems for the *FAST* simulations in the current study. The tower-base coordinate system is fixed in the support platform. It translates and rotates with the platform. The tower-top coordinate system is fixed to the top of the tower. It translates and rotates as the platform moves, but does not yaw with the nacelle [25]

Table A.1: Different momentums from the FAST simulations with a flow field from spectral analysis as well as from CFD simulations for the tower-top coordinate system at turbine 2

	Spectral Method		CFD Method	
Quantity	Mean	Std. Deviation	Mean	Std. Deviation
Roll Moment [kNm]	$3.01 \cdot 10^3$	270.46	$3.05 \cdot 10^3$	343.23
Pitch Moment [kNm]	391.7	554.85	219.22	629.94
Yaw Moment [kNm]	-3.73	505.89	142.72	586.98

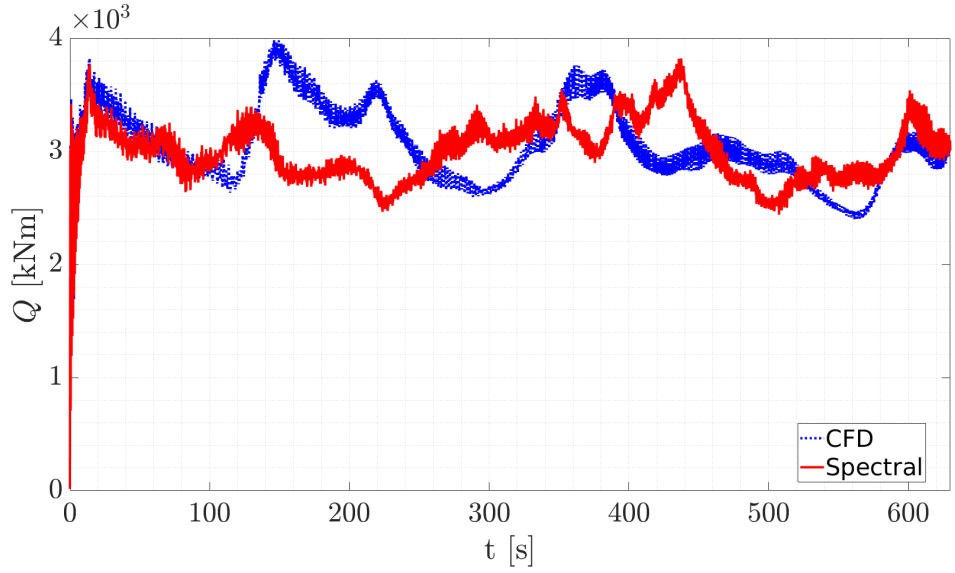

Figure A.2: Tower-top roll moment of turbine 2. It is aligned to the x-axis of the tower-top coordinate system.

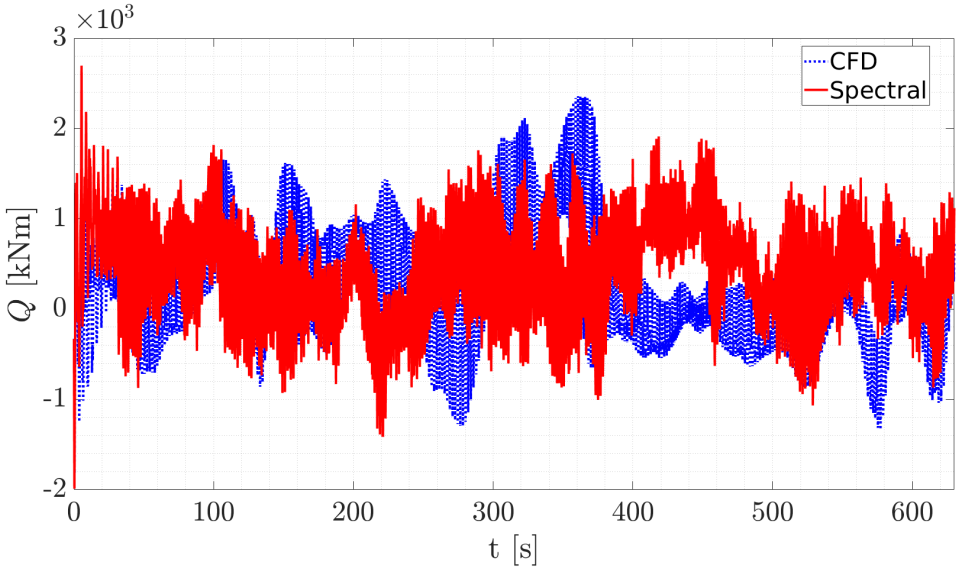

Figure A.3: Tower-top pitch moment of turbine 2. It is aligned to the y-axis of the tower-top coordinate system

Table A.2: Different momentums from the FAST simulations with a flow field from spectral analysis as well as from CFD simulations for the tower-based coordinate system at turbine 2

	Spectral Method		CFD Method	
Quantity	Mean	Std. Deviation	Mean	Std. Deviation
Roll Moment [kNm]	$3.23 \cdot 10^3$	$1.04 \cdot 10^3$	$3.11 \cdot 10^3$	897.01
Pitch Moment [kNm]	$4.62 \cdot 10^4$	$4.96 \cdot 10^3$	$4.62 \cdot 10^4$	$5.67 \cdot 10^3$
Yaw Moment [kNm]	-3.54	505.89	142.92	586.99

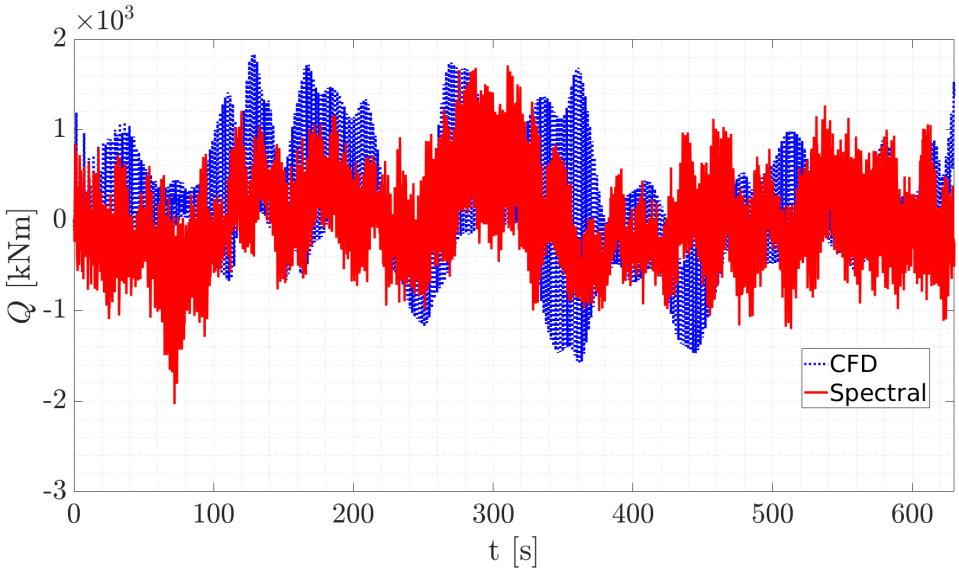

Figure A.4: Tower-top yaw moment of turbine 2. It is aligned to the z-axis of the tower-top coordinate system

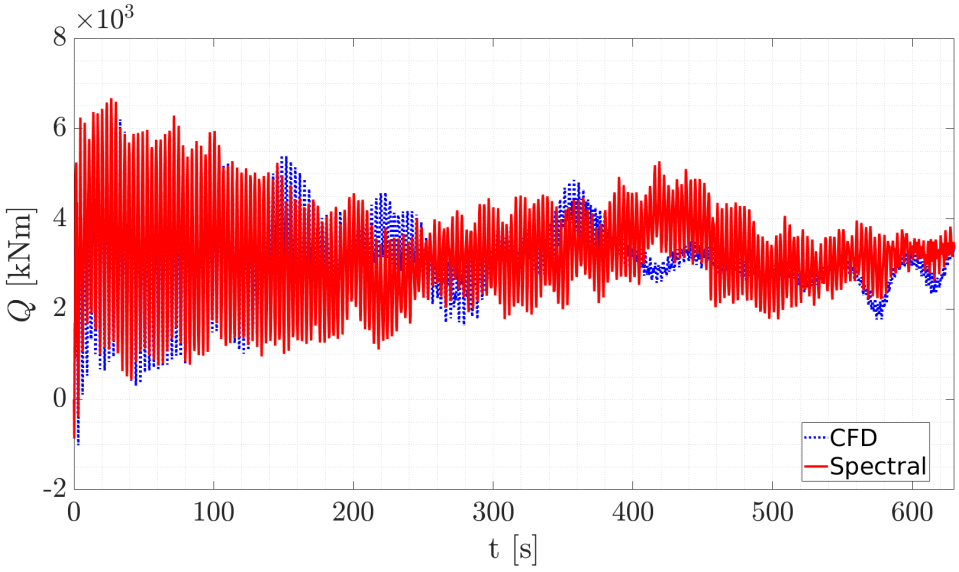

Figure A.5: Tower-based roll moment of turbine 2. It is aligned to the x-axis of the tower-base coordinate system

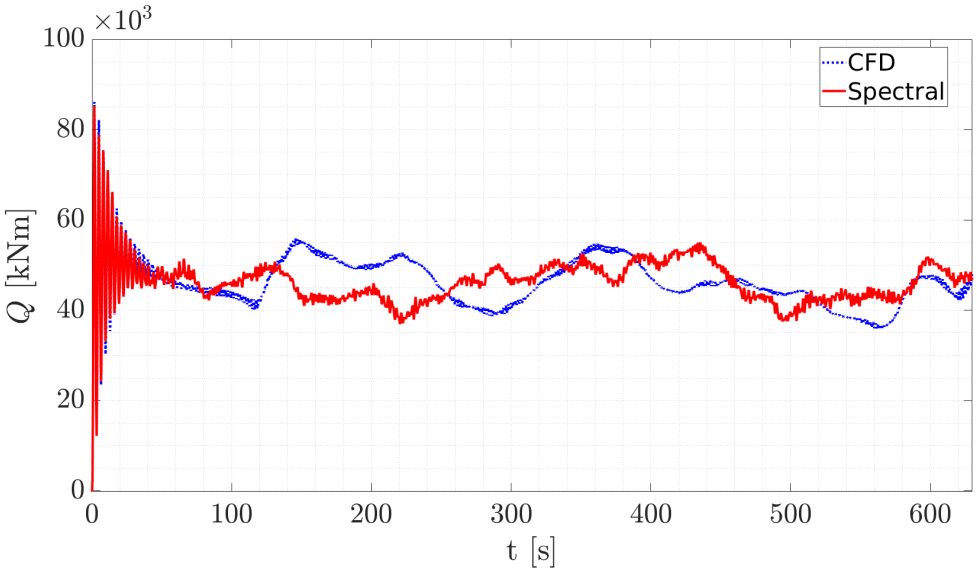

Figure A.6: Tower-based pitch moment of turbine 2. It is aligned to the y-axis of the tower-base coordinate system

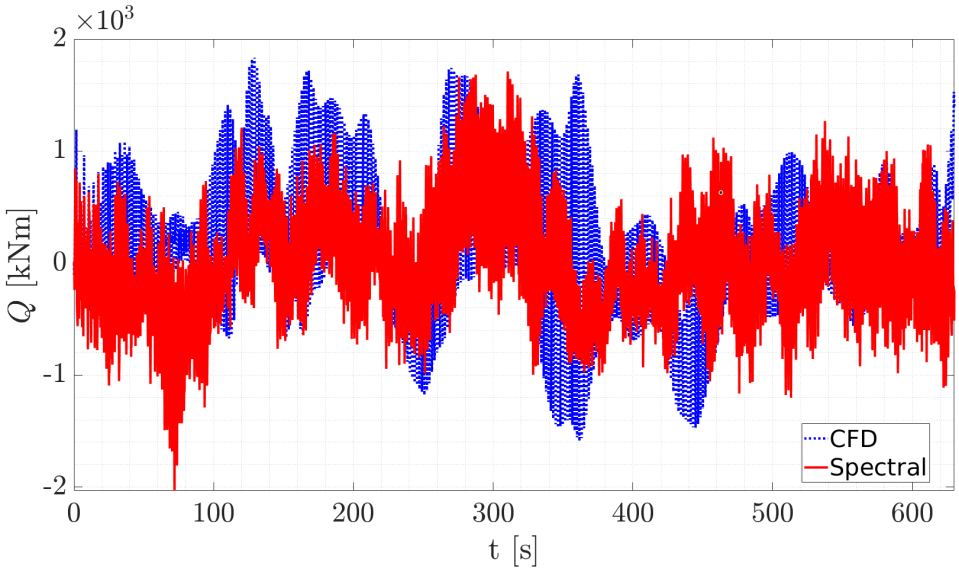

Figure A.7: Tower-based yaw moment of turbine 2. It is aligned to the z-axis of the tower-base coordinate system

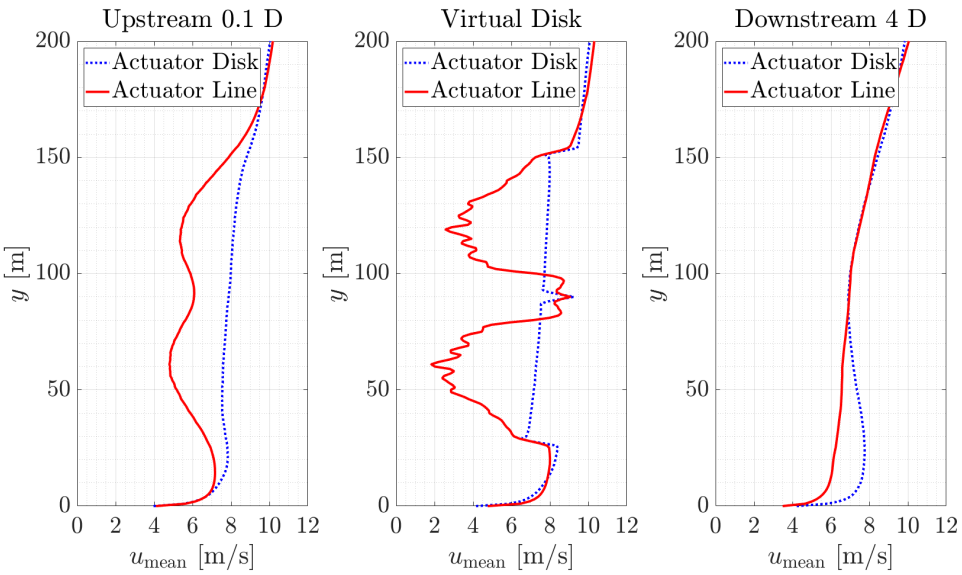

Figure A.8: Comparison of the streamwise velocity component between the Actuator Disk and Actuator Line simulation near turbine 2

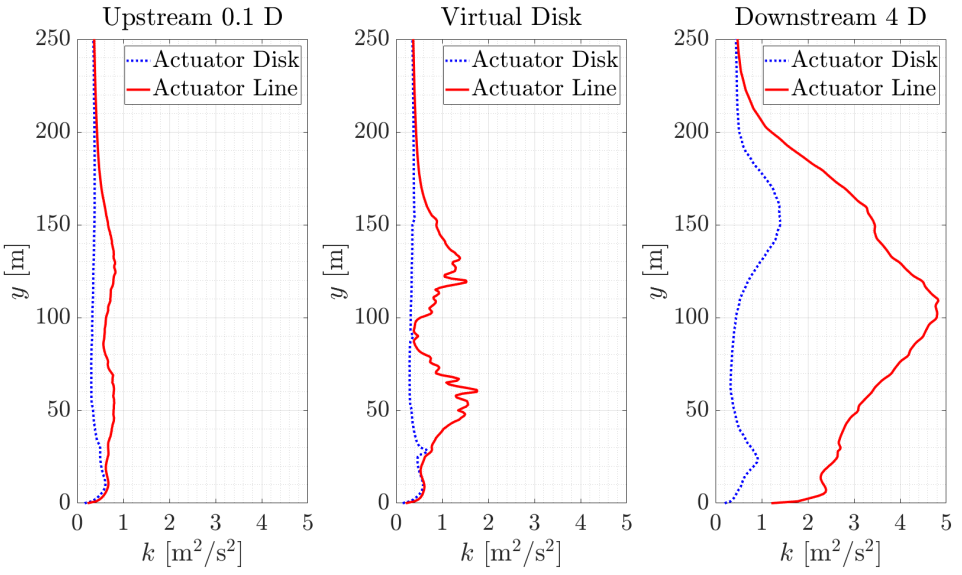

Figure A.9: Comparison of the turbulent kinetic energy between the Actuator Disk and Actuator Line simulation near turbine 1

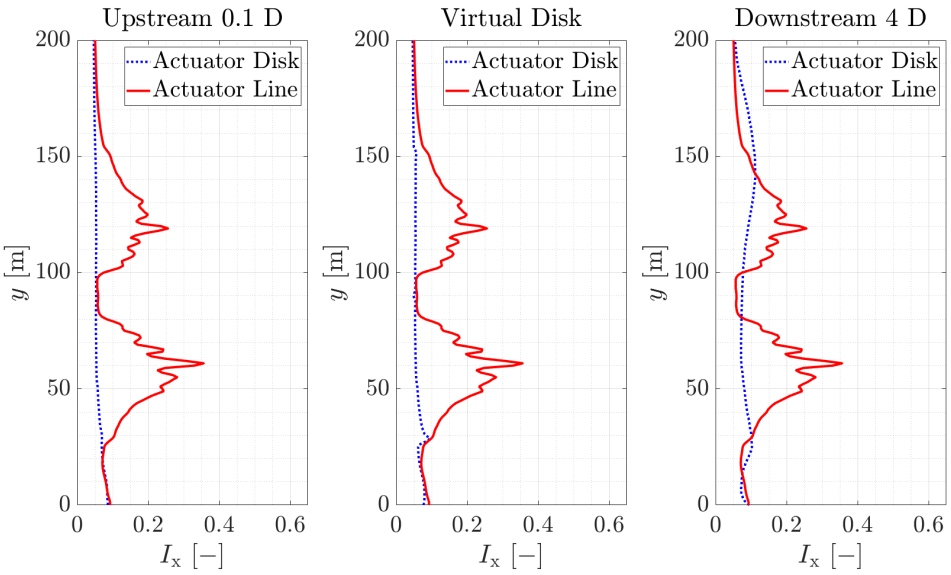

Figure A.10: Comparison of the turbulence intensity between the Actuator Disk and Actuator Line simulation near turbine 1

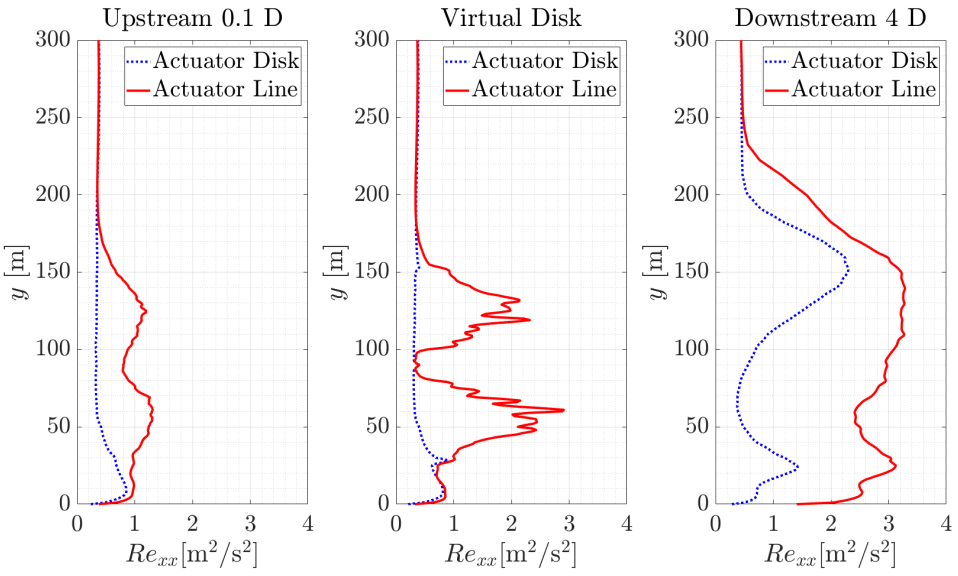

Figure A.11: Comparison of the streamwise normal component of the Reynolds stresses Re_{xx} between the Actuator Disk and Actuator Line simulation near turbine 1

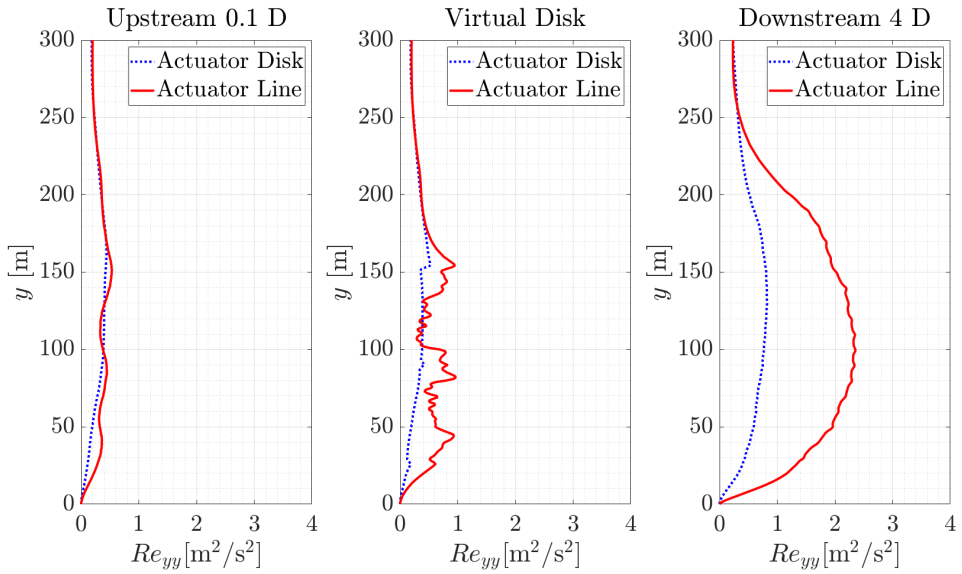

Figure A.12: Comparison of the normal component of the Reynolds stresses in the wall-normal direction Re_{yy} between the Actuator Disk and Actuator Line simulation near turbine 2

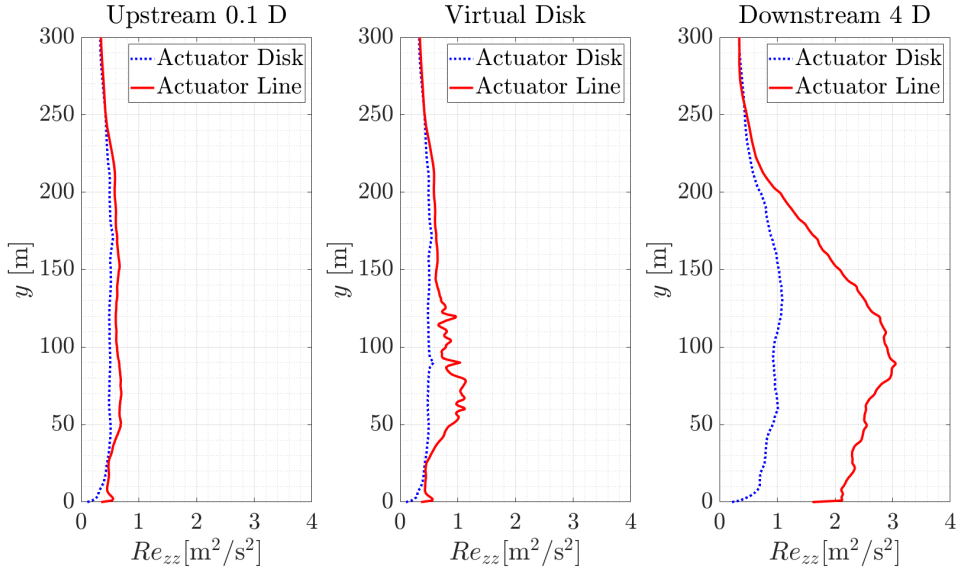

Figure A.13: Comparison of the normal component of the Reynolds stresses in the spanwise direction Re_{zz} between the Actuator Disk and Actuator Line simulation near turbine 2

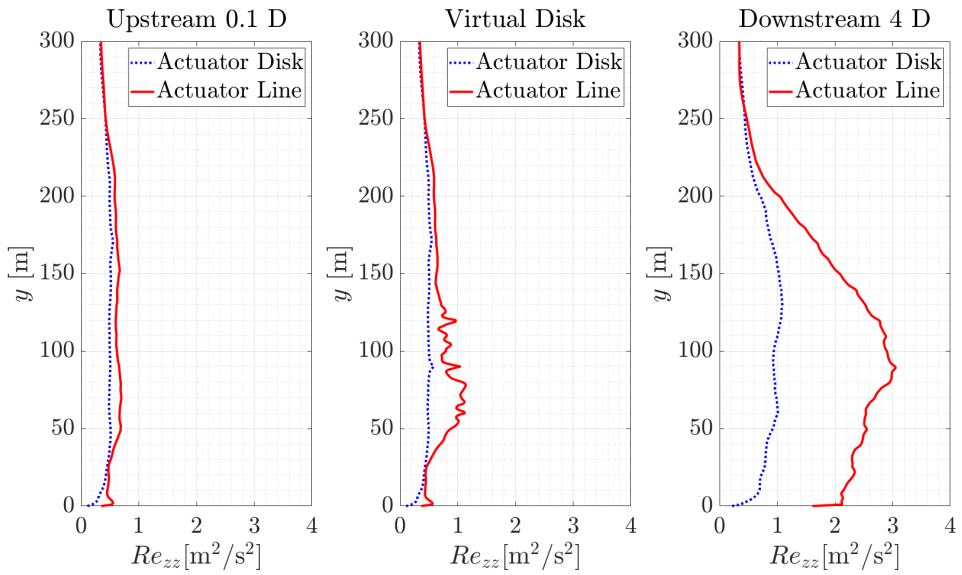

Figure A.14: Comparison of the shear component of the Reynolds stresses Re_{xz} between the Actuator Disk and Actuator Line simulation near turbine 2

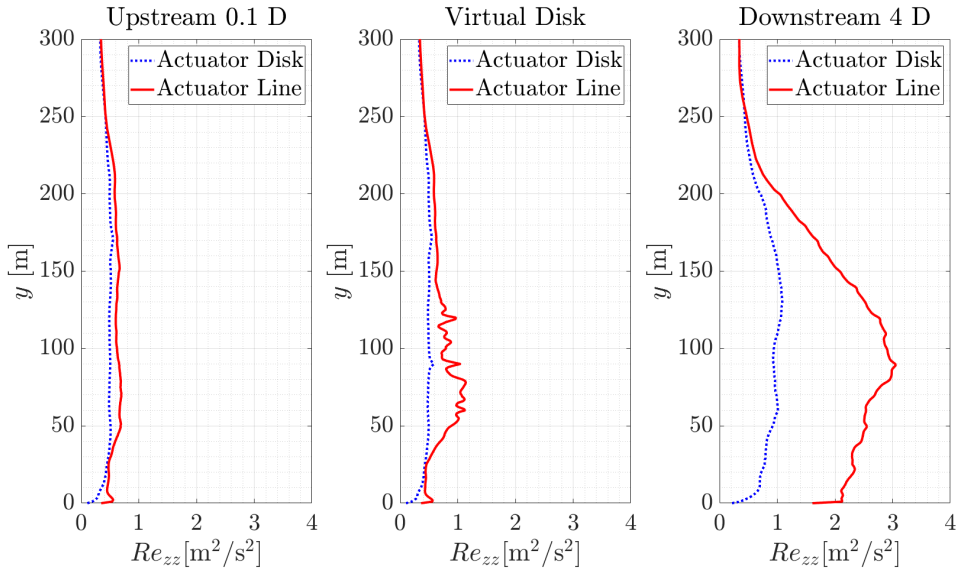

Figure A.15: Comparison of the shear component of the Reynolds stresses Re_{yz} between the Actuator Disk and Actuator Line simulation near turbine 2